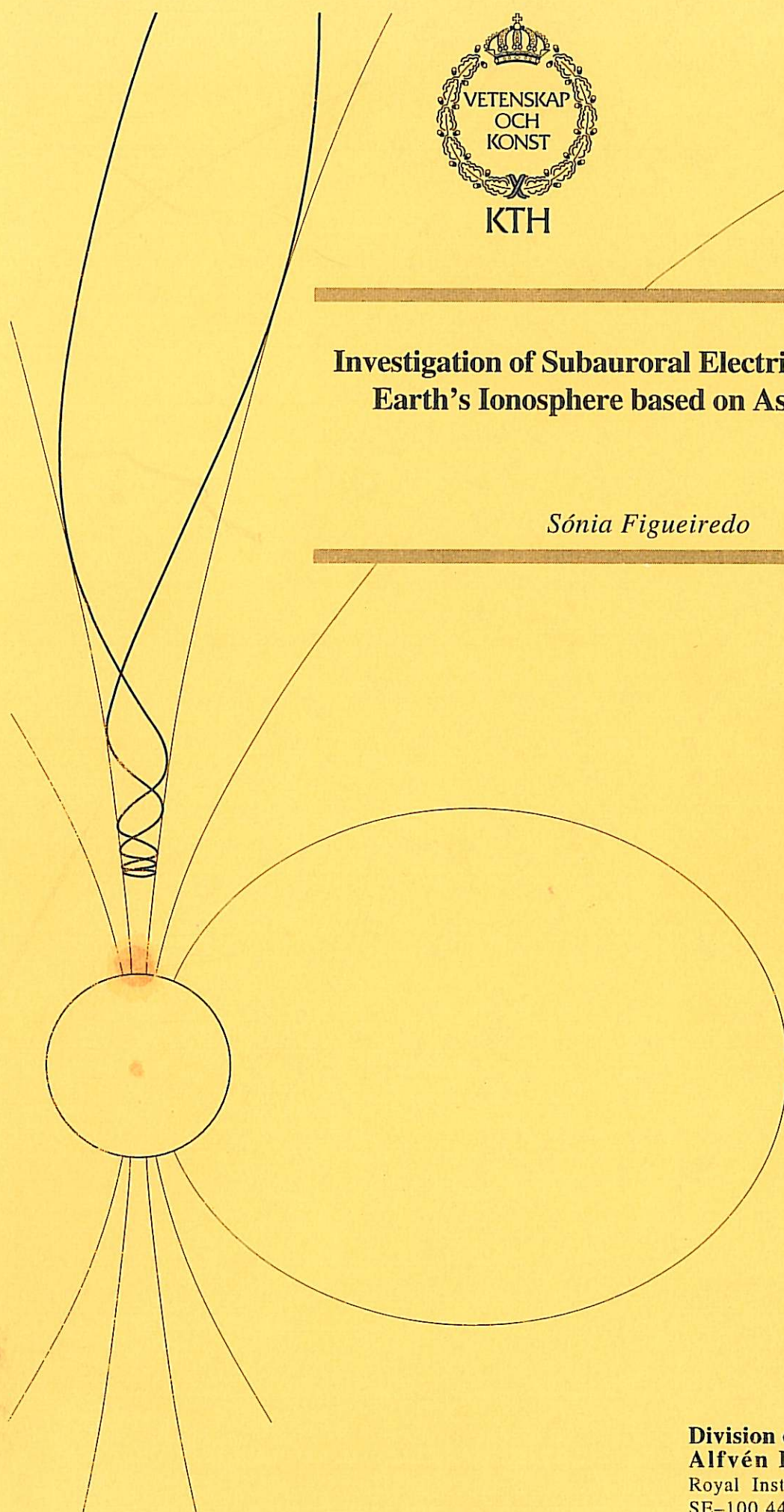




Investigation of Subauroral Electric Fields in the Earth's Ionosphere based on Astrid-2 data

Sónia Figueiredo



**Division of Plasma Physics
Alfvén Laboratory**
Royal Institute of Technology
SE-100 44 Stockholm, Sweden

**Investigation of Subauroral Electric Fields in the
Earth's Ionosphere based on Astrid-2 data**

Degree Thesis

**Instituto Superior Técnico
Technical University of Lisbon**

**carried out at
Alfvén Laboratory
Division of Plasma Physics
Royal Institute of Technology
Stockholm, Sweden**

**Sónia Figueiredo
Stockholm, May 2001**

List of Contents

1. Introduction to Fundaments of Space Physics	1
1.1. The Ionosphere	1
1.2. The Magnetosphere	4
1.3. The Solar Wind and its Interaction with the Earth's Magnetosphere	7
1.4. The Auroral Ionosphere	14
2. The Astrid-2 Satellite	18
3. Investigation of Subauroral Ion Drifts based on Astrid-2 Data	20
3.1. Statistical Study Results	20
3.1.1. Definitin of a SAID Event	20
3.1.2. Study of the Dependence of SAID Occurrence on Geophysical Parameters	22
3.2. Case Study Results	32
4. Discussion and Conclusions	45
Appendix	53
Acknowledgements	56
References	57

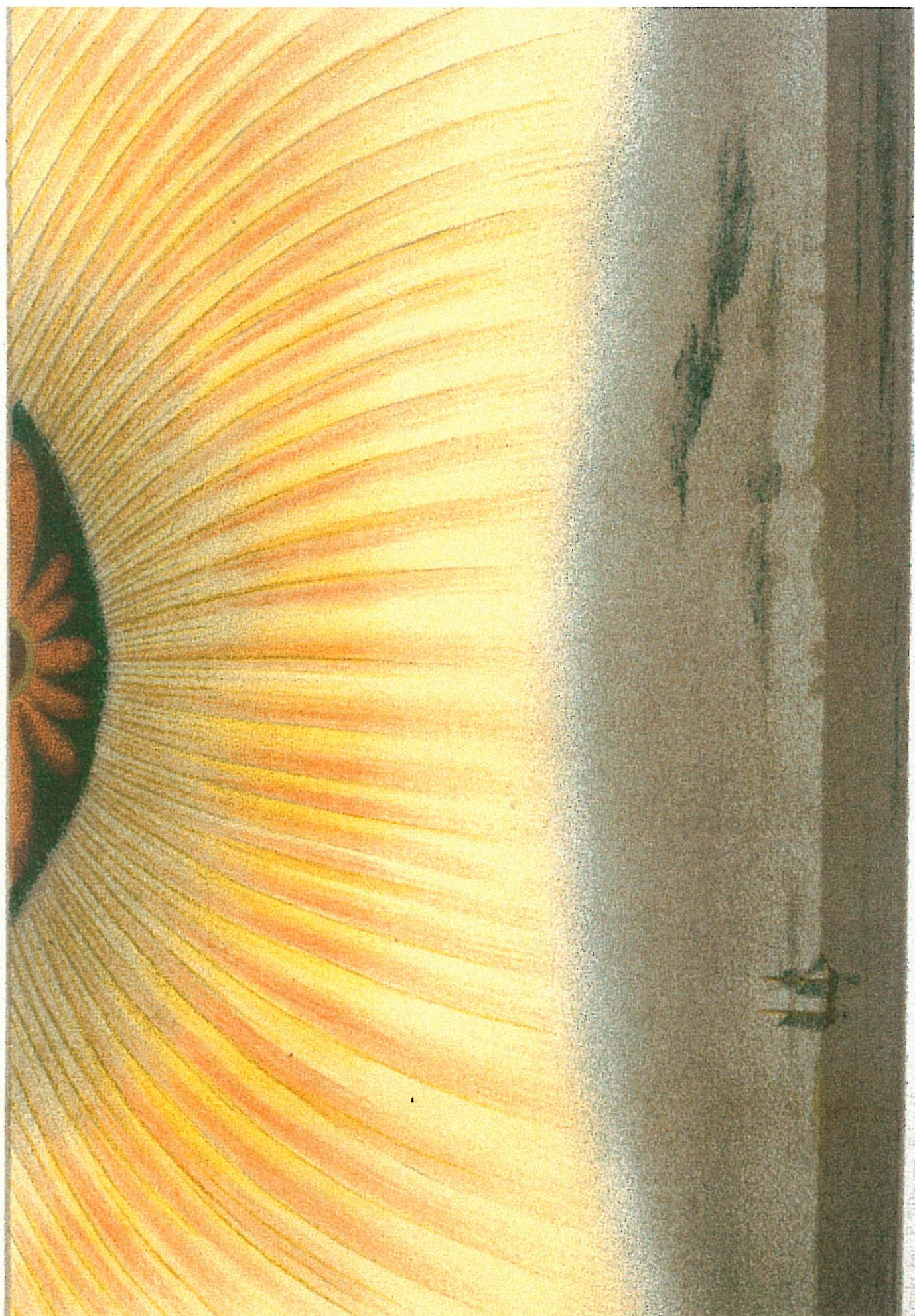
Abstract

The subject of this thesis work is the study of subauroral electric fields based on Astrid-2 satellite data.

A statistical study was done in order to analyse its spatial distribution and structure properties, as well as its dependence on some external geophysical parameters such as magnetic activity and substorm-related currents.

A more detailed study was done for some selected events, where field aligned and Pedersen currents were calculated. From these results height-integrated Pedersen conductivity profiles were obtained.

From the discussion of the results and from the comparison with previous proposed models for the generation mechanism of subauroral electric fields, conclusions were obtained and indicate the closure current system through the low density region of the midlatitude trough, as the responsible for the creation of these ionospheric intense electric fields.



1. Introduction to Fundamentals of Space Physics

1.1. The Ionosphere

The combination of a neutral gaseous medium with a source of ionization results in the formation of an electrically conducting medium.

The neutral medium of interest in this work is the upper atmosphere, and the sources of ionization are the radiation of the sun with wavelength range less than 2400 (UV and X-rays), particle radiation with energies of a few keV, and cosmic radiation (energy range between 10^8 and 10^{20} eV). The result is the ionosphere: an electrically conducting layer in the upper atmosphere.

Figure 1.1. shows the earth's dayside ionosphere (solid line) as well as the neutral atmosphere (dashed line) composition and density.

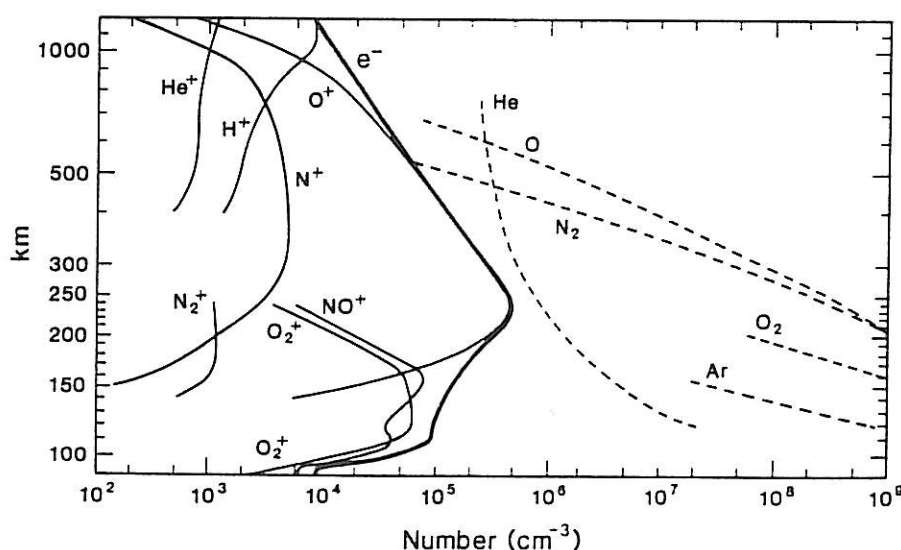


Figure 1.1.1.
International quiet solar year (IQSY) daytime
ionospheric and atmospheric composition.
(From Johnson, 1969.)

From comparison between the ionosphere density and the neutral atmosphere profiles it is seen that the earth atmospheric ionization is relatively weak showing although a significant variety with altitude in its structure.

Indeed, the substructure of the electron density profile led to the definition of three major ionospheric layers: D, E and F regions. This last layer is usually divided into F1 and F2 subregions. The major daytime electron density peak is located at approximately 250 km altitude — F2 region — as predicted by the Chapman profile, from the balance between the decrease of radiation intensity and the increase of atmospheric density with decreasing altitudes.

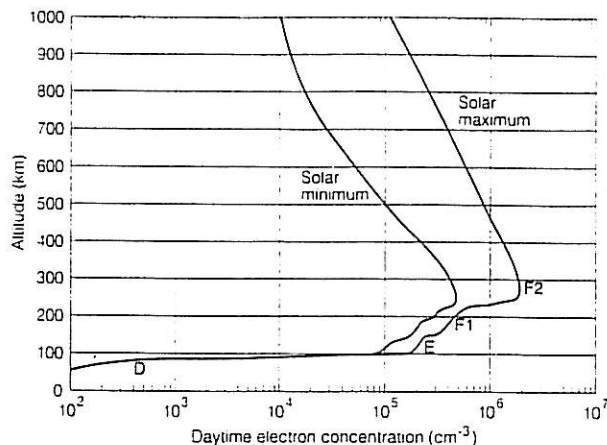


Figure 1.1.2.
Altitude distribution of electron density in
the ionosphere in the daytime.
(From Hanson, 1965.)

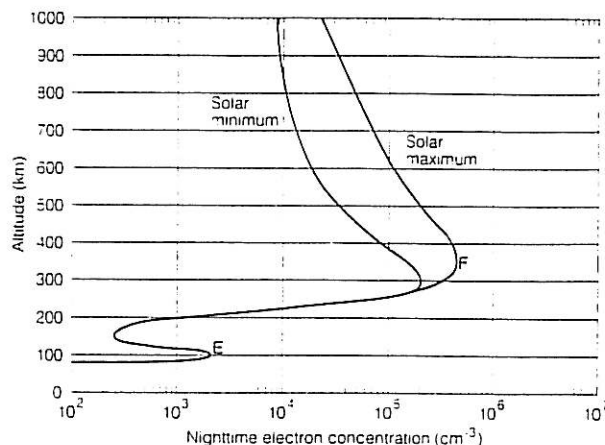


Figure 1.1.3.
Altitude distribution of electron density in
the ionosphere in the nighttime.
(From Hanson, 1965.)

Since the solar radiation is only present on the dayside and depends on the solar activity, the electron density varies with local time and solar activity, as it is shown on figures above.

Another important physical property that characterizes the ionosphere is the electrical conductivity. The ionospheric plasma shows a strong anisotropy in its conductivity, assuming considerably different magnitudes in different directions relative to the magnetic field.

Defining $\sigma_{//}$ as the conductivity in the direction parallel to the magnetic field, σ_P — Pedersen conductivity — parallel to the electric field component perpendicular to the magnetic field, and σ_H — Hall conductivity — which direction closes this axis system of reference, it is seen that the parallel conductivity is dominating, being at altitudes of 250 km about 10^5 times greater than the other components which are comparable between each other.

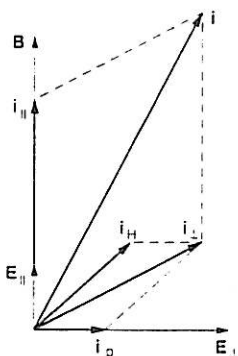


Figure 1.1.4.
Definition of $\sigma_{//}$, σ_P and σ_H .

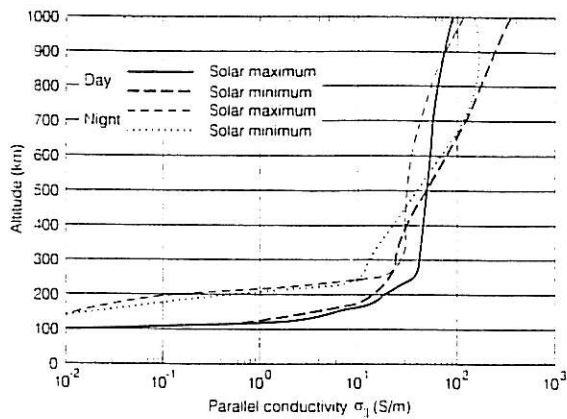


Figure 1.1.5.
Altitude variation of the parallel
conductivity in the ionosphere.
(From Hanson, 1965.)

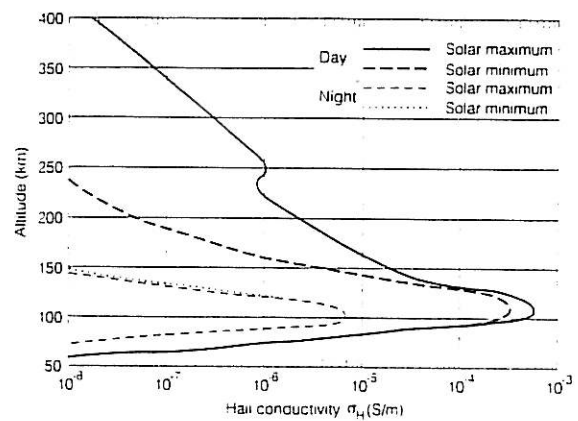


Figure 1.1.6.
Altitude variation of the Hall
conductivity in the ionosphere.
(From Hanson, 1965.)

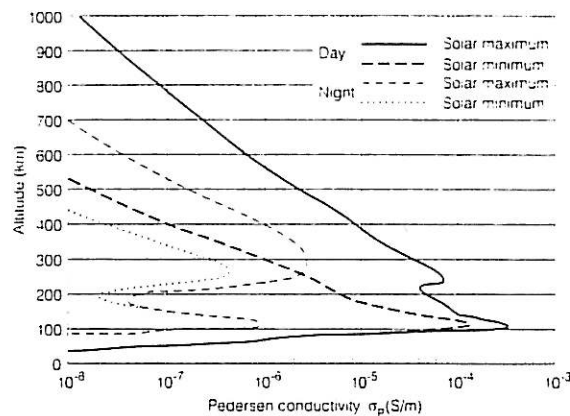


Figure 1.1.7.
Altitude variation of the Pedersen
conductivity in the ionosphere.
(From Hanson, 1965.)

The presence of a magnetic field that gives an electron cyclotron frequency much greater than the collision frequency have the consequence of the electrons diffusion being less on the transversal directions than on the longitudinal direction. In this way, the parallel conductivity is greater than the transversal conductivities.

It is also common to define height-integrated conductivity coefficients, when studying the large-scale ionospheric electrodynamics.

These are given by

$$\Sigma_P = \int_{z_l}^{z_u} \sigma_P \, dz \quad \Sigma_H = \int_{z_l}^{z_u} \sigma_H \, dz \quad (1.1.)$$

where z_l and z_u are the lower and the upper limits, usually assuming values between 70-90 km and 160-220 km, respectively.

1.2. The Magnetosphere

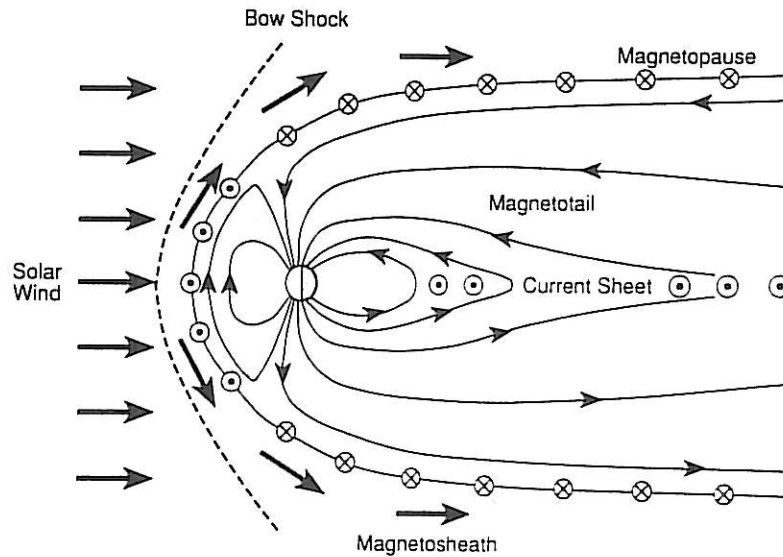


Figure 1.2.1.
View of the magnetosphere in the
noon-midnight meridian

The figure above shows a cross section of the magnetosphere in the noon-midnight meridian.

The *magnetosphere* is regarded as a cavity region in space where the geomagnetic field dominates. This cavity constitutes an obstacle to the supersonic flow of the solar wind (300 — 900 km/s) and so a bow shock is created in front of the magnetosphere. The solar wind is deflected and flows around the magnetopause, forming the *magnetosheath*.

The *magnetopause*, originally called Cahill discontinuity, is regarded as a thin boundary demarking the separation and interaction between the geomagnetic field and plasma of primarily terrestrial origin¹, and the solar wind plasma.

¹ This is highly debatable and still a topic of research.

The extended magnetic field lines in the nightside form the *magnetotail*. A thin current sheet flows across the midplane of the magnetotail and connects with the magnetopause currents at the flanks of the tail.

These magnetospheric current sheets are referred to as thin layers since their thickness is typically of the order of several hundred kilometres, while they extend for tens of Earth radii.

Nearer to the Earth there is a very sharp boundary (less than one Earth radius thick), called the *plasma* *pause*. This boundary limits a region of relatively dense plasma (10-100 particles per cubic centimetre) forming the *plasmasphere*.

Outside the *plasma* *pause*, mainly on the dayside, the plasma density can decrease to very low values. This region of low density is often referred to as the *trough*.

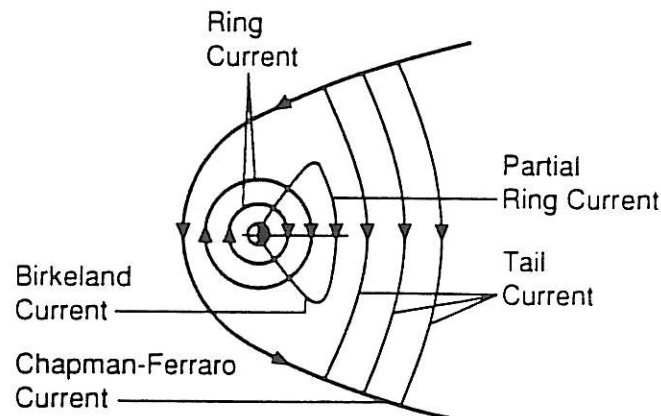


Figure 1.2.2.

Major types of currents in the earth's magnetosphere as seen from high above the North Pole.

This view of the magnetic equatorial plane shows the major types of currents in the earth's magnetosphere as seen from high above the North Pole.

The *Chapman-Ferraro current* flows eastward along the magnetopause, while across the center of the tail flows a westward *tail current* consistent with the stretched magnetic field geometry of the earth's magnetotail.

On the inner magnetosphere flows westward a *ring current* centered on the earth and created by particles drifting in the Van Allen radiation belts at distances of about 3-5 Earth radii. Additional *partial-ring currents* flow, which connect to the ionosphere via *Birkeland currents*.

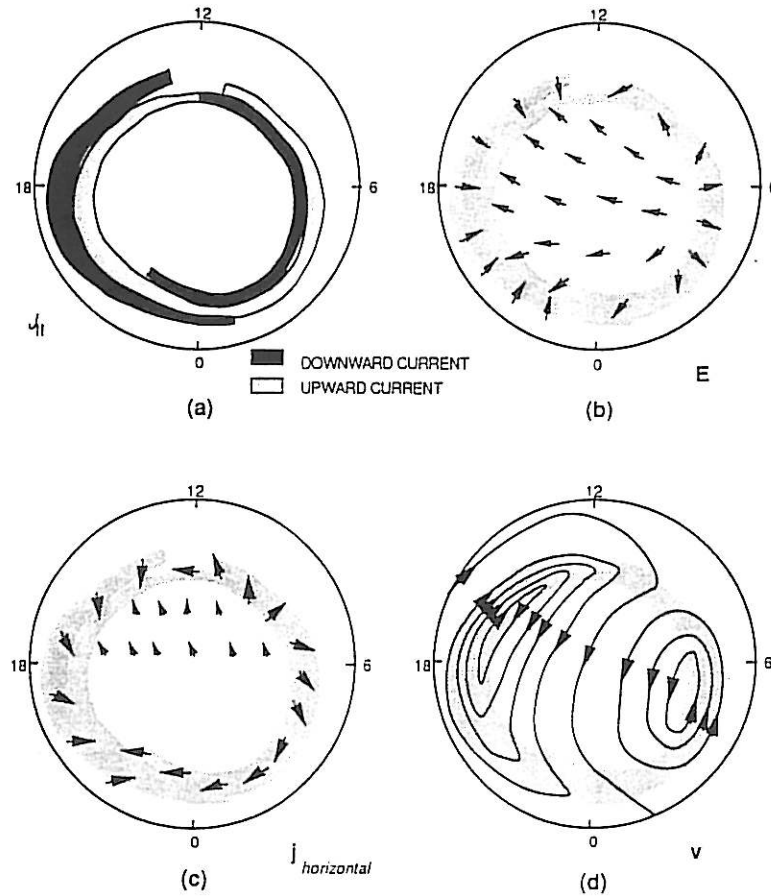


Figure 1.2.3.
Typical patterns observed in the earth's ionosphere,
as viewed from high above the North Pole.

This set of four pictures gives a view of some typical patterns characteristic of the ionosphere.

In the picture (a) is shown a distribution of Birkeland currents in magnetic latitude and local time, as viewed from high above the North Pole.

The poleward region of this current system is called region-1 Birkeland current, and it is directed upward on the dusk side and downward on the dawn side. The equatorward region is the region-2 Birkeland current, where the current directions are reversed relatively to the region-1 current system on both dusk and dawn sides.

The region where the current is flowing down into the ionosphere tend to charge up positively whereas the upward current charge up negatively, giving in this way, rise to the electric field pattern showed on picture (b).

In response to this electric field, ionospheric horizontal currents are created, consisting of a Pedersen current flowing parallel to the transversal (relative to \vec{B}) electric field and a Hall current flowing in the direction $-\vec{E} \times \vec{B}$. Since the Pedersen and Hall conductivities are comparable (as discussed in 1.1.), ionospheric currents tend to form an angle of about 45° with the transversal electric field.

On the nightside of the polar cap, due to the low ionospheric conductivity, the current flow is weak, while on the dayside the current flow is considerable.

The final diagram represents both equipotential curves and $\vec{E} \times \vec{B}$ drift flow, since the drift direction $\vec{E} \times \vec{B} = \vec{B} \times \nabla\phi$ is perpendicular to equipotential curves.

1.3. The Solar Wind and its Interaction with the Earth's Magnetosphere

As a result of the big difference in gas pressure between the solar corona and the interstellar space, an ionized solar plasma —*solar wind*— is driven outward from the Sun, escaping even from its gravitationally bound atmosphere.

The solar wind consists mainly of nearly equal densities of protons and electrons (ionized hydrogen), a small percentage of ionized helium (about 5 % but can occasionally rise up to more than 20 %), and even less of heavier elements.

It is also characterized by a magnetic flux since, due to its high electrical conductivity, a magnetic field *frozen in* to this plasma is transported with direction nearly parallel to the ecliptic plane, and forming an angle of approximately 45° in respect to a line directed from the Sun to an observer at the orbit of the Earth. This interplanetary magnetic field, *IMF*, with intensity varying between 3-30 nT, is not only derived from currents in the Sun, but it is also due to electric currents in the solar wind itself.

In the tables 1.3.1. and 1.3.2. are shown some measured properties of the solar wind at a distance of one *astronomical unit* ($1\text{AU} = 1.5 \times 10^{13} \text{ cm} = 2.5 \times 10^4 R_E$) from the Sun, i.e., near the location of the Earth's orbit.

Proton density	6.6 cm^{-3}
Electron density	7.1 cm^{-3}
He^{2+} density	0.25 cm^{-3}
Proton temperature	$1.2 \times 10^5 \text{ K}$
Electron temperature	$1.4 \times 10^5 \text{ K}$
Flow speed (nearly radial)	450 km/s
Magnetic field (induction)	$7 \times 10^{-9} \text{ T}$

Table 1.3.1.
Typical solar wind parameters near the orbit of the Earth.

	Flux Density	Flux Through Sphere at 1 AU
Protons	$3.0 \times 10^8 \text{ cm}^{-2} \cdot \text{s}^{-1}$	$8.4 \times 10^{35} \text{ s}^{-1}$
Mass	$5.8 \times 10^{-16} \text{ g} \cdot \text{cm}^{-2} \cdot \text{s}^{-1}$	$1.6 \times 10^{12} \text{ g} \cdot \text{s}^{-1}$
Kinetic energy	$6 \times 10^{-8} \text{ J} \cdot \text{cm}^{-2} \cdot \text{s}^{-1}$	$1700 \text{ J} \cdot \text{s}^{-1}$
Thermal energy	$2 \times 10^{-9} \text{ J} \cdot \text{cm}^{-2} \cdot \text{s}^{-1}$	$50 \text{ J} \cdot \text{s}^{-1}$
Magnetic energy	$10^{-9} \text{ J} \cdot \text{cm}^{-2} \cdot \text{s}^{-1}$	$25 \text{ erg} \cdot \text{s}^{-1}$
Radial momentum	$2.6 \times 10^{-9} \text{ Pa}$	$7.3 \times 10^{14} \text{ N}$
Radial magnetic flux	$5 \times 10^{-9} \text{ T}$	$1.4 \times 10^{15} \text{ Wb}$

Table 1.3.2.
Solar-wind flux densities and fluxes near the orbit of the Earth.

The following table shows some derived properties of the solar wind near the orbit of the Earth.

Gas pressure	30 pPa
Sound speed	60 km/s
Magnetic pressure	19 pPa
Alfvén speed	40 km/s
Proton gyroradius	80 km
Proton-proton collision time	4×10^6 s
Electron-electron collision time	3×10^5 s
Time for wind to flow from corona to 1 AU	4 days = 3.5×10^5 s

Table 1.3.3.

Some derived properties of the solar wind near the orbit of the Earth.

The numbers show that the solar wind carries mass away from the Sun at a rate of $1.6 \times 10^{12} \text{ g} \cdot \text{s}^{-1}$ which, even over 5-billion-yr lifetime, is negligible compared with its $2 \times 10^{33} \text{ g}$ mass.

Also the comparison between the total energy flux ($1.775 \times 10^{27} \text{ erg} \cdot \text{s}^{-1}$) transported by the solar wind with the radiated energy from the Sun ($4 \times 10^{33} \text{ erg} \cdot \text{s}^{-1}$), confirms that this outward plasma flux from the Sun has negligible effect in its overall mass and energy balance.

Nevertheless, its interaction with the Earth magnetic environment has an important role and its fundamental principles will be briefly discussed below.

As mentioned above, the cavity that encloses the terrestrial magnetic field constitutes an obstacle to the solar wind flow. Indeed, it is the balance between its dynamic pressure or momentum flux as well as its magnetic and thermal pressure, and mainly the magnetic pressure in the magnetosphere, that determines the location of the magnetosphere limit.

Since the dynamic pressure or momentum flux of the solar wind is equal to $\rho_{\text{sw}} \cdot u_{\text{sw}}^2$, where ρ_{sw} represents the density of the solar wind and u_{sw} its velocity, and being the magnetic pressure of the magnetosphere equal to $\frac{B_{\text{ms}}^2}{2\mu_0}$, the pressure balance equation is expressed by the equality

$$\rho_{\text{sw}} \cdot u_{\text{sw}}^2 = \frac{B_{\text{ms}}^2}{2\mu_0} \quad (1.2.)$$

However, passing through the shock and the magnetosheath, the intervenients on this balance equation change since the solar wind flow is now tangential to the magnetopause, and so the inexistence of normal stresses makes the dynamic pressure contribution being zero. At this level, the balance is done only between the magnetic

pressure of the inner magnetosphere and the magnetic and thermal pressures of the solar wind.

Even at the nose of the inner magnetosphere, the solar wind pressure is about 11 % less than the dynamic pressure of the incident solar wind, felt outside the magnetosheath.

As a result from this pressure balance, the dayside magnetosphere extent is estimated to be around 8 - 12 Earth radii from the center of the Earth. The elongated shape on the nightside of the magnetospheric cavity is also a consequence of the solar wind flow, and the tail width is determined by the balance between the tail magnetic pressure and the solar wind thermal and magnetic pressures.

Another effect of the interaction between the solar wind and the geomagnetic field is the process called *reconnection*.

The *frozen in flux* criterium states that in a fluid characterized by high conductivity (diffusion effects negligible) the field lines move together with the fluid, i.e., field lines are regarded as material lines: two elements of matter linked by a common field line will remain linked by that field line as the fluid moves and deforms through space.

This coupling between material motion and magnetic field is valid when the *magnetic Reynolds number* — relation between magnetic convection and diffusion, $R_M \approx \mu_0 \sigma u L$ — is much greater than unity. L is a characteristic dimension of the observed system, in this case the size of the magnetospheric cavity (8 — 12 R_E), and u a typical magnetospheric flow speed (100 km/s), R_M is about 10^{11} , and so this criterium surely holds.

But, looking to the relatively thin current sheets such as the magnetopause, where L assume a value of some hundreds of kilometres, the frozen in criterium and the magnetohydrodynamics theory break down locally. In the regions called diffusion regions, where R_M is less than unity, magnetic field lines are not tied up to the plasma and a process called *reconnection* can occur. This phenomenon is illustrated on the figure below.

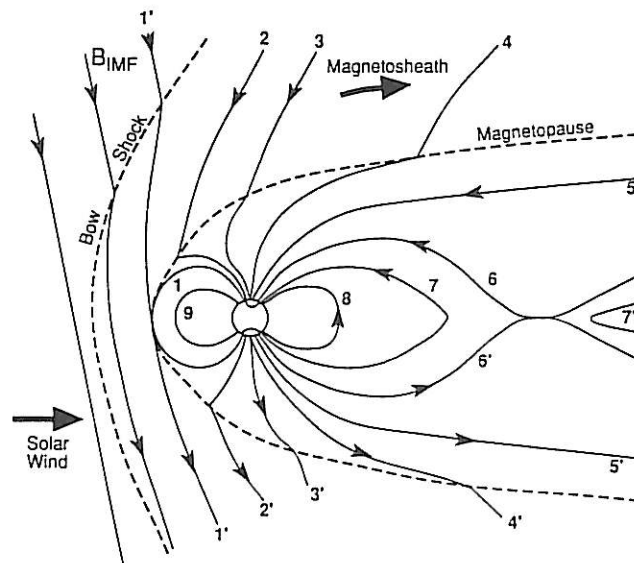


Figure 1.3.1.
Illustration of magnetic reconnection occurring in the magnetosphere.

When the original magnetic field line (represented by 1) transported by the solar wind reaches the thin current sheet of the magnetopause, it reconnects with the geomagnetic field line, as shown schematically is below.

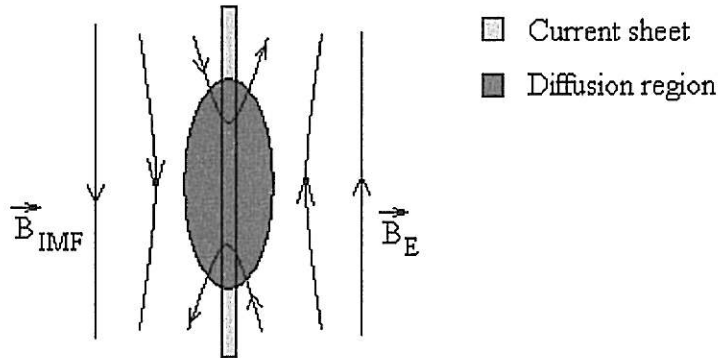


Figure 1.3.2.
Simplified picture of the magnetic reconnection mechanism.

Due to the reconnection process flux tubes containing different plasma populations can connect to each other and the different populations can mix and interact.

Is this interaction between the interplanetary magnetic field driven by the solar wind and the Earth's magnetosphere that explains the convection of plasma, and so, mass, energy and momentum, within the magnetosphere. However, this injection of momentum and energy will depend on the direction of the IMF. Whenever the IMF is southward, i.e., antiparallel to the Earth magnetic field in the equatorial plane, the particle and energy injection, which occurs mainly in the cusp region, becomes stronger, since it has an opposite direction relative to the geomagnetic field. The reason for this is that the reconnection process is more efficient for anti-parallel magnetic fields (see figure 1.3.2.)

Besides the relative magnetic field lines directions, the amount of magnetic flux that reconnects depends on the rate at which the solar wind transports flux to the Earth. This rate is given by $u \cdot B_{IMF} \sin \theta$, where θ is the angle formed between the direction of the IMF and the solar wind direction of motion (in the geocentric solar magnetosphere coordinate system, GSM, $B_{IMF} \sin \theta$ is the z-component, considering u parallel to the x-direction). This quantity is also equal to the magnitude of the solar wind electric field that is created according to the electrodynamics principle that states *an electric conductor moving with velocity \vec{u} , in a magnetic field \vec{B} , gives rise to an electric field given by $\vec{E} = -\vec{u} \times \vec{B}$* . Its direction is from the morning side to the evening side of the magnetosphere (dawn to dusk).

In this way, the solar wind can also be regarded as a magnetohydrodynamic generator with an electromotive force of the order of 100 kV.

Combining this generator function of the solar wind with its efficiency on the power releasing in the magnetosphere, we can picture that the magnetosphere behaves almost as if it were a simpler rectifier with its conduction direction from dawn to dusk: solar wind electric field direction from dawn to dusk is implied by an IMF southward, which corresponds to intense release of power.

This picture is confirmed by measurements as shown below.

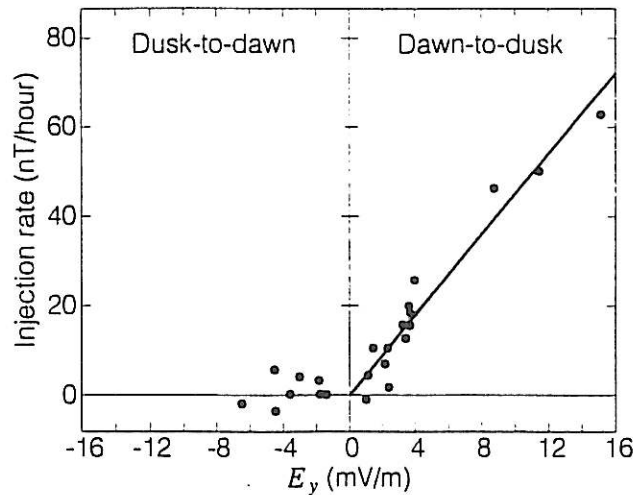


Figure 1.3.3.

Power released in the magnetosphere as a function of the y -component of the interplanetary electric field. (From Burton *et al.*, 1975)

The interaction of the solar wind with the Earth's magnetosphere is not restricted to the effects above described. One of those not yet mentioned is the occurrence of disturbances in the geomagnetic field at the Earth's surface. Such disturbances are called *geomagnetic activity*.

As figure 1.2.2. shows, there are in the magnetosphere different current systems. These currents flowing above the ionosphere are strongly influenced by the solar wind, mainly by its dynamic pressure, which depends on the solar wind velocity and density, and by the dawn-dusk component of the solar wind electric field, which depends on the velocity and on the north-south component of the IMF. The occurrence of changes in any of these controlling parameters will induce changes in strength, location and distribution of the currents. Consequently changes in the magnetic field are detected at the Earth's surface.

These disturbances mainly affect the horizontal component of the geomagnetic field, and a disturbance of the order of 1000 nT represents between 2% and 8 % of the horizontal component magnitude at the equator ($B_H \approx 62 \mu\text{T}$) and in regions of high latitude ($B_H \approx 13 \mu\text{T}$), respectively. When the geomagnetic field is strongly disturbed — periods known as *geomagnetic storms* — practical effects such as on radio communications, radar observations and synchronous spacecraft, can be detected.

The study of geomagnetic activity as well as the study of phenomena occurring on the Sun, has shown that the Sun is the original source of these perturbances, with the solar wind being its vehicle of transport.

There are two main controlling parameters: the solar wind velocity and the southward component of the IMF. It has been found that some activity indices increase as the square of the solar wind velocity, existing only if the IMF has southward component. There is no activity predicted for northward IMF.

Attempts have been made to develop prediction procedures of the magnetic activity strength. However, studies have shown that at time scales of less than 3h, only about half of the variance in magnetic activity indices is predictable. The unpredictable fraction is related to a suddenly release of energy stored in the magnetosphere due to interaction with the solar wind. These discrete events are known as *magnetospheric substorms*.

A definition of substorm can be stated as following,

A substorm is the ordered sequence of events that occur in the magnetosphere and ionosphere when the IMF turns southward and increased energy flows from the solar wind into the magnetosphere.

(McPheron, 1979, 1991; Akasofu, 1979; Rostoker *et al.*, 1980)

Figure 1.3.4. shows, through the representation of two magnetic activity indices (*AU* and *AL*), which are the envelopes of the superposed H-component traces from a worldwide chain of magnetometers², the evolution phases of a particular magnetospheric substorm.

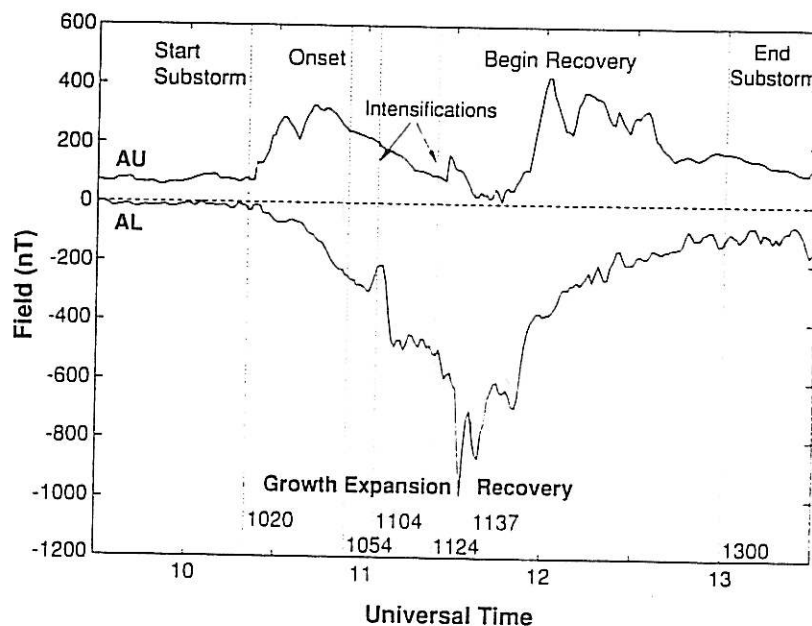


Figure 1.3.4.

AU and AL indices for a particular studied substorm (From McPheron and Manka, 1985)

From the analysis of the slope of the AL curve three main phases of the substorm may be defined: *growth*, *expansion* and *recovery phases*. As it can be seen through this example, a substorm can last for 3 hours.

Once the substorm starts, the magnetosphere undergoes a sequence of several changes in its magnetic field and plasma properties. During the period of time of the *growth phase*, a configuration change of the nightside geomagnetic field lines occur,

² More detailed information about this definition will be presented later on.

resulting in an even more tail-like shape. This modification means that strong electric currents from dawn to dusk are present (*cross-tail current*), and magnetic energy extracted from the solar wind is stored in the deformed magnetosphere. A period of time follows when this stored energy is released or unloaded — the *expansion phase*. After approximately 90 minutes from the start of the substorm, the *recovery phase* begins and mainly consists on the return of the magnetosphere to its ground state.

The figure below is a schematic representation of the several current systems linking magnetospheric and ionospheric currents which are ultimately responsible for magnetic activity.

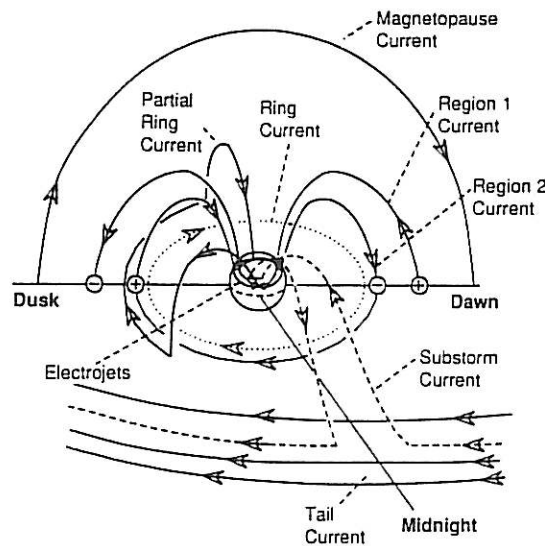


Figure 1.3.5.
Representation of the various current systems

Shown are also two current systems not yet introduced: the *substorm current wedge* and the *auroral electrojets*.

The *substorm current wedge* is originated by the tail field collapse which has a consequence that the cross-tail current is linked into the midnight ionosphere through field-aligned currents, closing as a westward current filament in the ionosphere and then returning to space. The ionospheric portion of these current systems flow in enhanced-conductivity channels at high latitudes and are called the *auroral electrojets*. It is by means of the auroral electrojets that the stored energy is dissipated in the ionosphere during the expansion phase. Its fall takes place in the early recovery phase. The labelled intensifications in the AL index curve of Figure 1.3.3. are a consequence of the formation of new substorm current wedges and respective westward closing currents through the ionosphere.

To make the study of magnetic activity easier, standard indices were introduced giving us an idea of the intensity level of the disturbances.

The range index *Kp* and the substorm indices *AU*, *AL*, *AE* and *AO* will be briefly introduced here.

The index Kp is defined as the *arithmetic average of standardized values that nominally measures the magnitude of disturbances caused by phenomena other than the diurnal variation and the long-term components of the storm time variation measured at 13 standard observatories.*

The auroral-electrojet indices correspond to a measure of the strength of the auroral electrojets. The AU (auroral upper) index is defined at any instant of time as the maximum positive disturbance recorded by any station in the chain. AL is defined as the minimum disturbance defined by the lower envelope of the traces plotted with respect to a common baseline.

The AE index is defined as being $AE = AU - AL$, and AO as the average of AU and AL , $AO = \frac{AU + AL}{2}$.

1.4. The Auroral Ionosphere

One of the most amazing visible manifestations of the Earth's ionosphere electrodynamics is the *aurora*. Admired since long time, it continues to attract the curiosity of sky-observers and fascinating why?-minded people.

The auroral emissions are a consequence of the interaction between energetic particles, originating from the Sun and also from the Earth's atmosphere, and the atmospheric constituents.

These energetic particles arrive to the Earth's upper atmosphere moving along the magnetic field lines. In this way the occurrence of aurora is more probable in regions surrounding the geomagnetic poles, the so called *auroral zones*. They are defined as *the ones where on average over a long time the probability of occurrence of auroras is the greatest*. However, at a given instant in time, the geographic distribution of auroras is represented by the *auroral oval*. It is essentially fixed in space, being its enlarged region located on the nightside.

The boundary of these zones is approximately located around 60... in corrected geomagnetic latitude.

The figure below is an idealized representation of the rate of precipitation of auroral particles into the upper atmosphere.

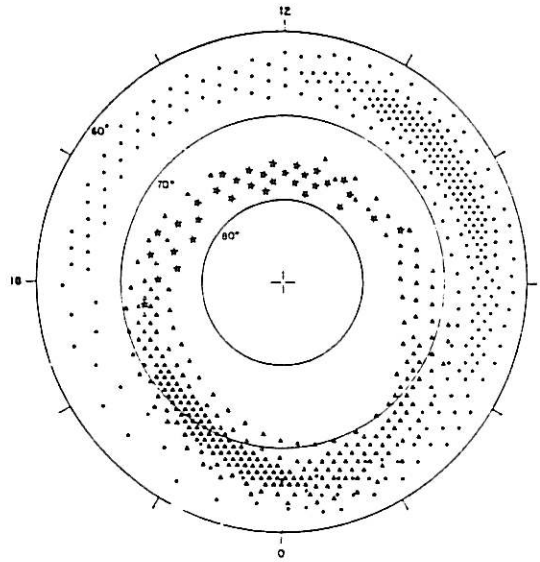


Figure 1.4.1.
Representation of the auroral particle precipitation pattern.

The triangles represent the auroral-oval precipitation, mainly composed by particles with energies in the range $\sim 0.5 - 20$ keV, responsible for visible aurora. The dots represent the region where the precipitation of high-energy (> 20 keV) auroral particles occur —auroral zone —, while the stars stand for the low energy particles (< 1 keV) constituting the polar-cusp precipitation that causes the dayside oval aurora.

From the interaction between the precipitating particles and the atmospheric constituents, auroral emissions in the ultraviolet, visible and infrared spectrum ranges results.

In Figure 1.4.2. it is shown an altitude distribution of the intensity of some auroral emission lines. The distribution is plotted for both day and night conditions.

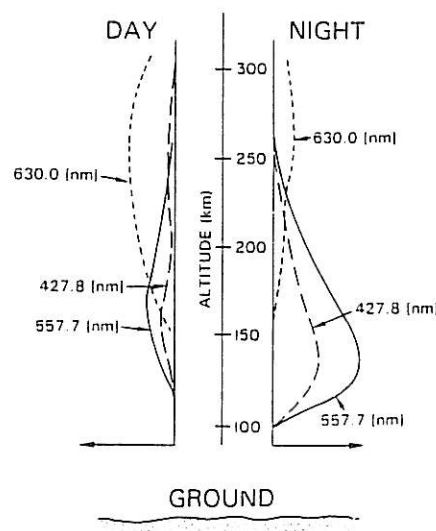


Figure 1.4.2.
Main differences between dayside and nightside auroras versus altitude.

The brightest visible emission corresponds to the green line at 557.7 nm, and is due to a des-excitation transition of atomic oxygen. This emission is dominant at low altitudes. The red line at 630 nm is the predominant one at high altitudes and also results from a des-excitation transition occurring on the atomic oxygen. Another spectrum line of significant intensity is the 427.8 nm line, at the blue end of the spectrum, and is a consequence of a N_2^+ transition.

The auroral emissions display is usually a combination of several different elementary forms. Some of them are illustrated below.

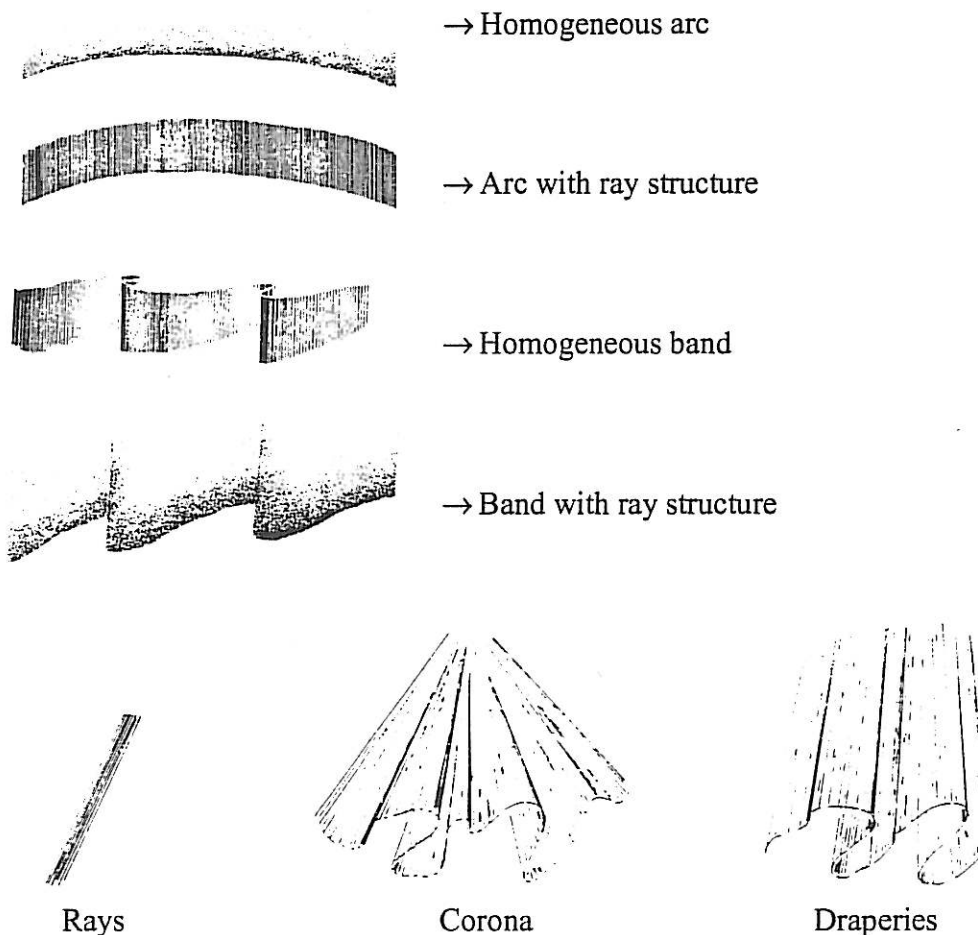


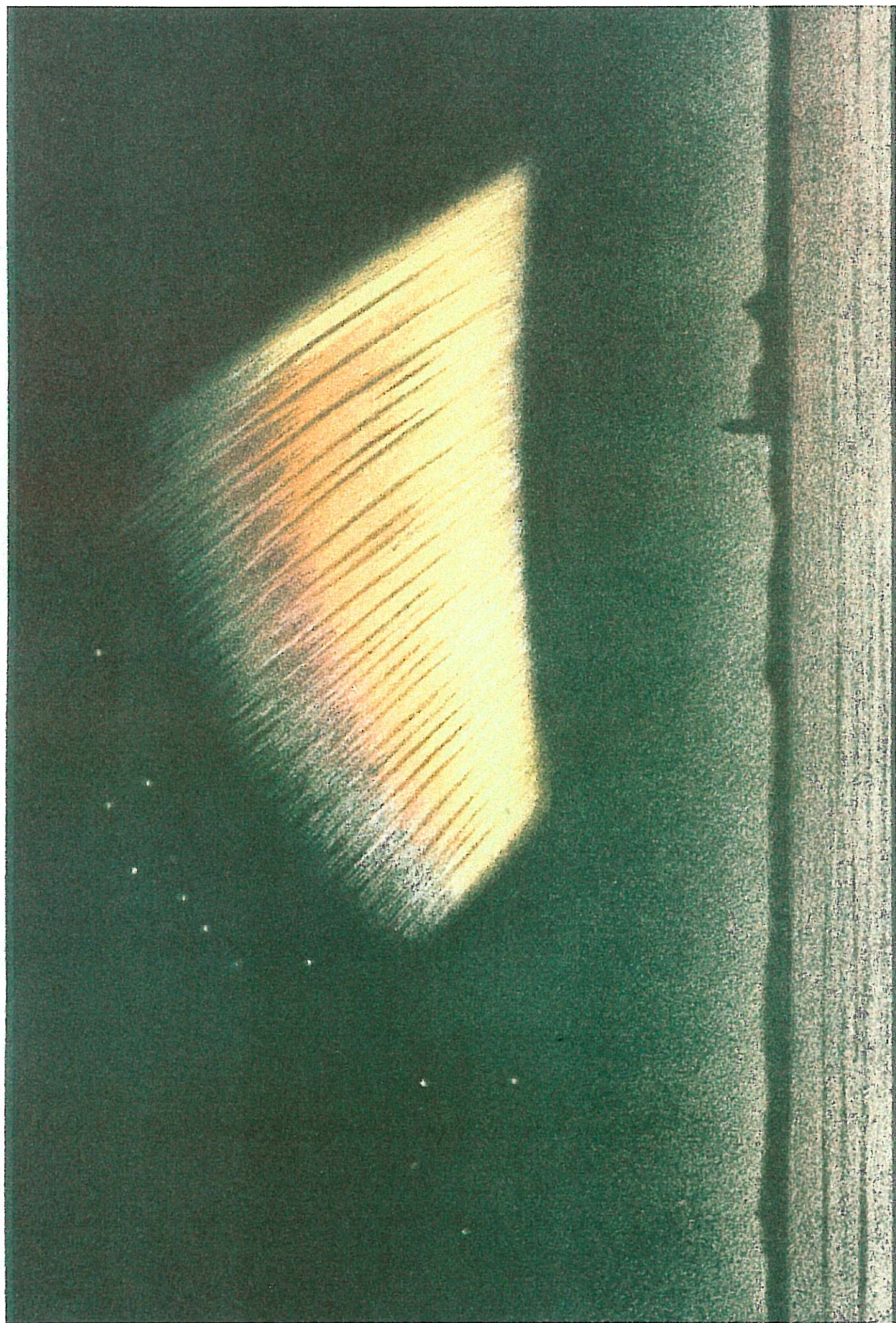
Figure 1.4.3.
Illustrations of typical forms of the northern lights.

Even being the auroral phenomenon the subject of many studies for a long time, there are still some mechanisms behind it not yet completely understood.

One of these is the mechanism responsible for the energization of the precipitating particles. Several different theories were presented explaining possible mechanisms for the auroral particle acceleration. However, all of them point out that it is a parallel electric field (parallel to the magnetic field) that accelerates the electrons, while the ions are also affected by transverse energization processes due to their larger Larmor radii. What each theory present as different is the process that generates the parallel electric field.

A summary list of these theories was presented by *André et al.* [1993], and is reproduced here.

1. Double layers [e.g. *Block*, 1972] are produced as a local plasma instability when the plasma contains an insufficient number of charge carriers. They constitute cavities with polarization on each side, frequently with a net voltage across. They have been studied in laboratories for more than 30 years and have now also been observed in space [*Temerin et al.*, 1982; *Boström et al.*, 1987].
2. Magnetic mirroring [e.g. *Alfvén and Fälthammar*, 1963] utilizes the magnetic mirroring forces as a current limiter. For instance, when the current carried by electrons in the loss-cone is insufficient for closing the current loop driven by the magnetospheric dynamo, part of the dynamo voltage will progress to lower altitudes. This will both open up the loss-cone and accelerate the source electrons.
3. Collisionless thermoelectric fields [*Hultqvist*, 1971] were proposed to exist as a result of the temperature difference between the hot magnetospheric and cold ionospheric plasma.
4. Anomalous resistivity [*Papadopolous*, 1977] was introduced to overcome the apparent infinite conductivity along magnetic field lines. The resistivity should occur as particles collisions with waves produced as a result of a current driven instability.
5. Alfvén waves [*Goertz and Boswell*, 1979; *Haerendel*, 1980, *Temerin et al.*, 1986] have been used to model a temporal/spatial variation of the field aligned particle acceleration. The process can be used to describe time variations of parallel potentials [*Haerendel*, 1983] or can be considered a generically independent acceleration process [e.g. *Temerin et al.*, 1986].
6. Lower hybrid waves [*Bingham et al.*, 1984] have been proposed as an alternative to the electrostatic acceleration of electrons. Waves generated by downward propagating magnetospheric ions are here assumed to accelerate electrons downward in a phased or quasi randomly fashion.



2. The Astrid-2 Satellite

The present thesis reports an investigation study based on measurements made by different instruments on-board of Astrid-2 satellite.

The Astrid-2 mission was developed by the Alfvén Laboratory of the Royal Institute of Technology in collaboration with the Swedish Space Corporation, being its two main objectives the diagnostic of auroral processes in the Earth's upper atmosphere and ionosphere, and the flight-test of innovative mechanisms included by the first time on-board of an auroral microsatellite.

Astrid-2 was launched in December 1998 as a piggy-back on a Kosmos-3M launcher from Pletsetsk in Russia. Its operational phase started on January 11, 1999 and finished on July 24, 1999. With a circular orbit at 1000 km altitude, an inclination of 83 deg and with a nodal regression rate relative to the Sun of -1.7 deg/day, it was possible to have a complete coverage of all local time sectors every 3.5 months. The spacecraft is spin-stabilized with a nominal rate of 10 rpm and the period of the orbit is 105'5".

Its payload was constituted by 5 scientific instruments:

EMMA — Electric and Magnetic Monitoring Aurora.

LINDA — Langmuir Interferometry and Density experiment for Astrid-2.

MEDUSA — Miniaturized Electrostatic Dual-tophat Spherical Analyzer.

PIA — Photometer for Imaging the Aurora.

ASC — Advanced Stellar Compass

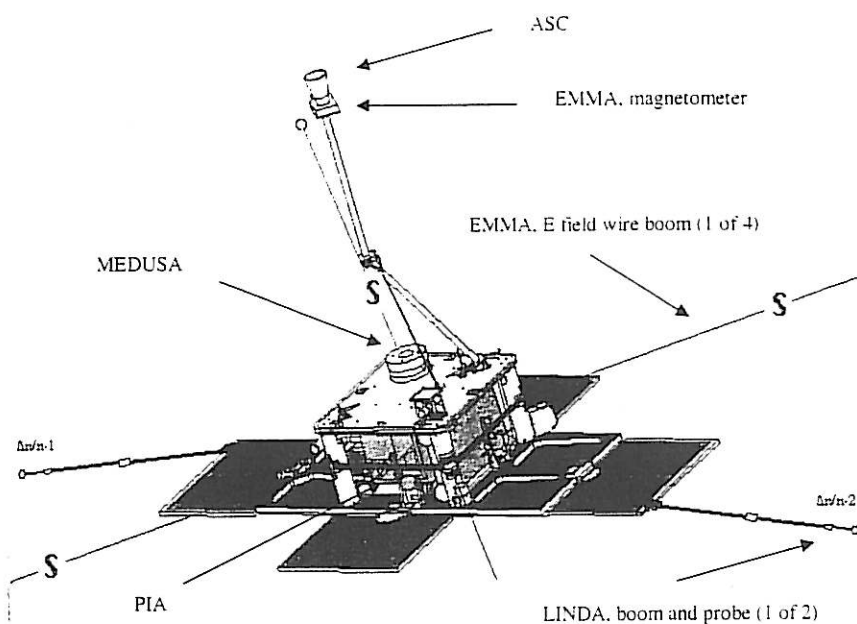


Figure 2.1.
The Astrid-2 platform and instruments

EMMA was an integrated electric field and magnetic field instrument measuring the two spin plane components of the electric field and the full magnetic field vector. For the electric field measurements four electric field probes mounted on wire booms in the spin plane were used, and for the magnetic field measurements, a tri-axial flux-gate magnetometer sensor mounted on an axial boom facing away from the Sun.

The spacecraft potential was continuously monitored by the electric probes and, when the probes were swept in current or voltage, a current-voltage characteristic could be obtained, from which information about the plasma density and temperature results. Also information about low-energy particles can be obtained, due to its attraction or repulsion movement relative to the spacecraft, if this is at a different potential from that of the plasma.

Sampling may be done at 16, 256 or 1048 samples/s. The range of measured electric field is ± 5 mV/m and the bit resolution is 0.2 mV/m. The magnetic field range is ± 65.536 nT and the bit resolution is in this case 0.125 nT.

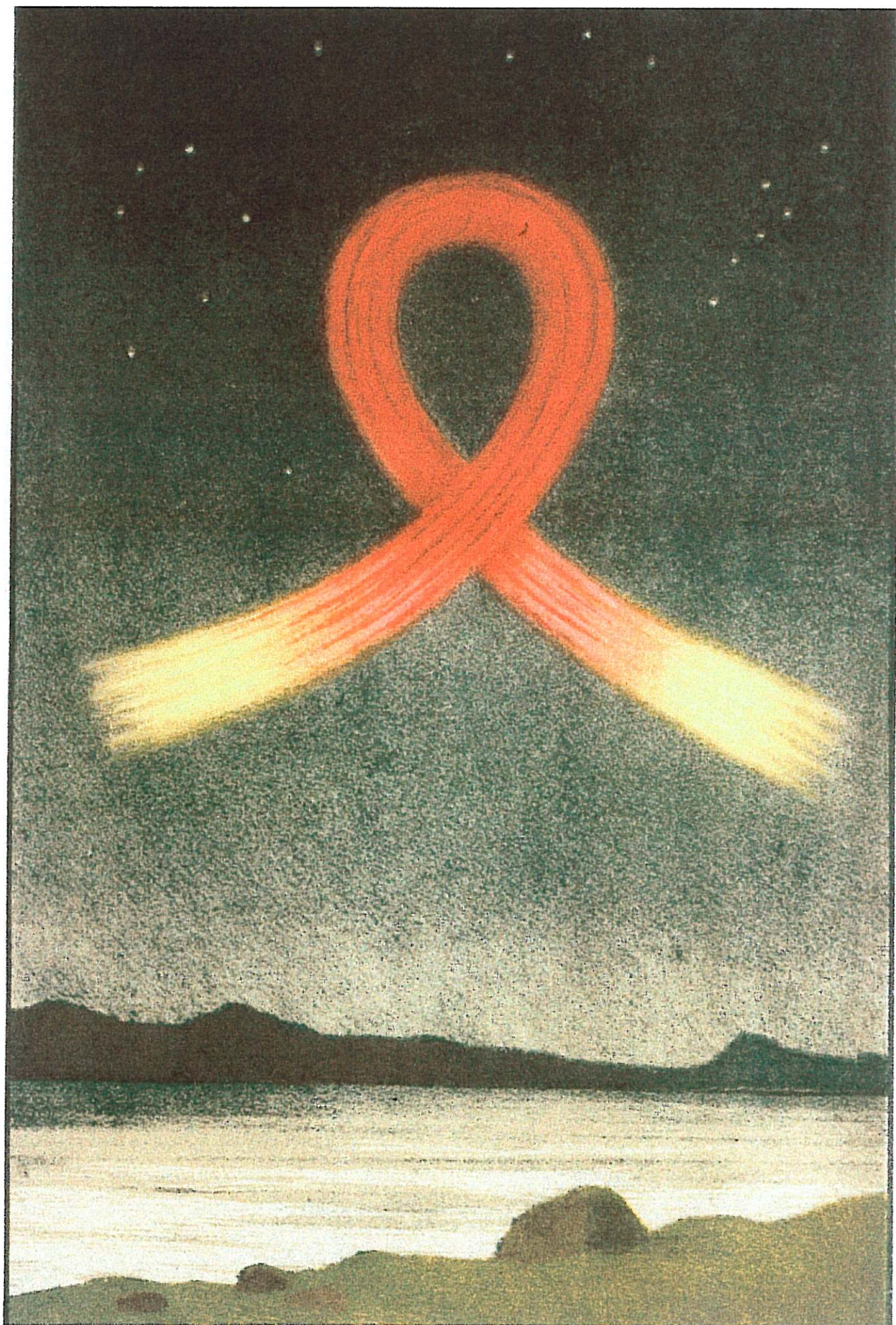
LINDA measured plasma density at up to 16 samples/s and density fluctuations at up to 8192 samples/s, which corresponds to a spatial resolution of about 1 meter. Using two Langmuir probes interferometric measurements of moving plasma structures were possible.

MEDUSA gave simultaneous information about energy of ions and electrons in the spacecraft spin plane. The maximum particle energy detectable is 18 keV per unit charge. For electrons up to 16 energy sweeps/s can be made. For ions the sampling rate is 8 sweeps/s.

PIA consisted of three photometers being two of them mounted in the spin plane for spin-scanning imaging of auroral emissions.

ASC determined the absolute values of the attitude avoiding the need of post-processing on the ground.

However due to technical problems, the operational phase of both PIA and ASC was short.



3. Investigation of Subauroral Ion Drifts based on Astrid-2 Data.

The main objectives of this thesis project are:

- Statistical study based on approximately six months of Astrid-2 electric and magnetic field data.
- Study of the relation between the occurrence and properties of subauroral ion drift events (SAID) and several geophysical parameters, such as magnetic local time (MLT), corrected geomagnetic latitude (CGLAT) and level of geomagnetic activity (Kp index and auroral electrojets indices).
- More detailed case study, where a calculation of the magnetospheric field aligned and Pedersen currents is made, as well as of the height integrated Pedersen conductivity.
- Discussion of the ionospheric response to magnetospheric currents as a possible generation mechanism of subauroral electric fields (SAEF), based on a comparison with previous proposed mechanisms.
- Presentation of summary and conclusions

3.1. Statistical Study Results

3.1.1. Definition of a SAID Event

In this investigation a subauroral ion drift event — SAID — is defined as poleward electric field with an intensity greater than 30 mV/m (which corresponds to a drift velocity of 1000 m/s), with a latitudinal extension between 0.05° and 1.05° (corresponding to a structure size between 5 and 105 km), located between 50° and 70° corrected geomagnetic latitude and equatorward of the auroral oval.

In order to apply this definition criterion to each orbit data of a set of 143 available orbits, which were chosen by manual inspection, an IDL programme was written to check if each orbit contains an event obeying to the predefined criterion.

Figure 3.1. is one example of a SAID event and shows schematically how this definition criterion is applied.

Astrid-2 data 1999-05-13 (DOY 133)

Orbit 16476

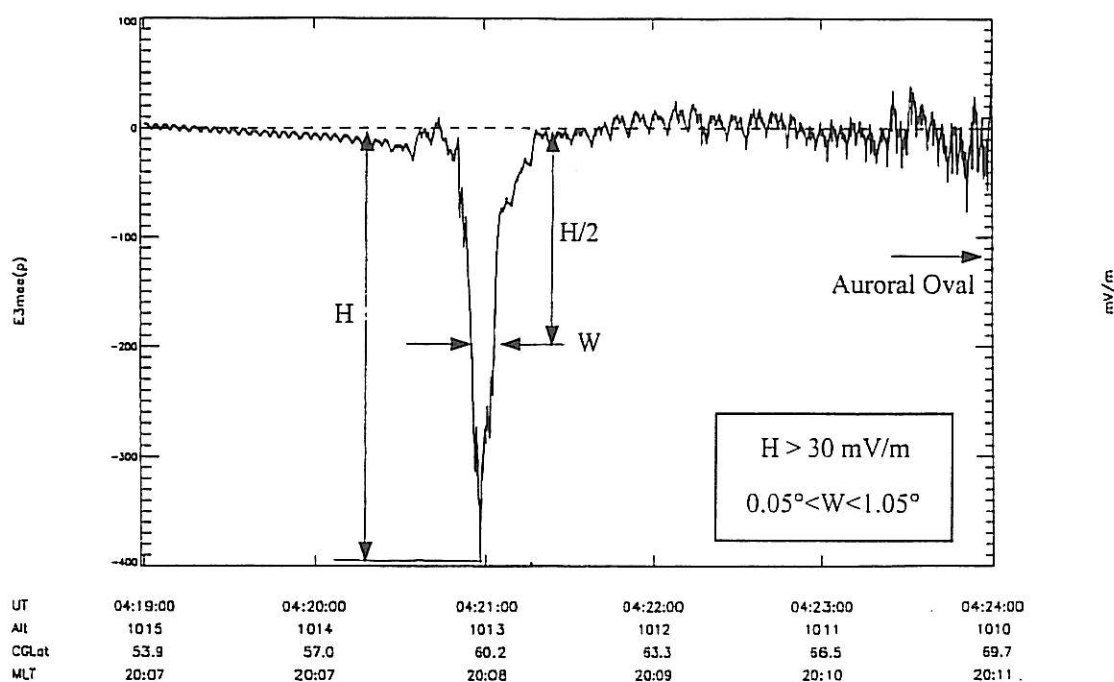


Figure 3.1.

Example of application of the SAID definition. The electric field component shown corresponds to the equatorward component.

As a result of this automatic inspection, a file with 72 selected orbits and respective SAID event identification parameters (MLT, CGLAT, electric field components, full width at half maximum, day of year, universal time, date) was created, and is the basis of the following study.

A manual inspection of the non-selected orbits was made with the purpose of finding out which was the main reason for not being considered as containing SAID events. The results show that 82 % of the non-selected orbits contained a poleward electric field peak with intensity greater than 30 mV/m but with structure width not between the defined limits. Of these 82 %, approximately 60% had a structure width smaller than the lower defined limit. Reasons such as the presence of noise disturbances and oscillations seem to be responsible for the generation of these peaks. Cases of weak poleward electric field peaks, as well as equatorward peaks, were found in smaller percentages.

Although the coverage of the satellite was similar for both hemispheres, from the set of 72 selected orbits, 47 correspond to events detected on the Southern Hemisphere while only 25 were found on the Northern Hemisphere.

3.1.2. Study of the Dependence of SAID Occurrence on Geophysical Parameters.

Defining the SAID occurrence probability at a given region of the CGLat — MLT space, as the ratio between the number of detected events and the number of satellite passages correspondent to that space region, a polar plot of the distribution of occurrence probability over the CGLat-MLT space was done.

For the calculation, the CGLat-MLT space was divided into bins with latitudinal extension of 5° and 1 hour in MLT.

The resulting plot as well as a polar plot showing the coverage of the satellite are presented below.

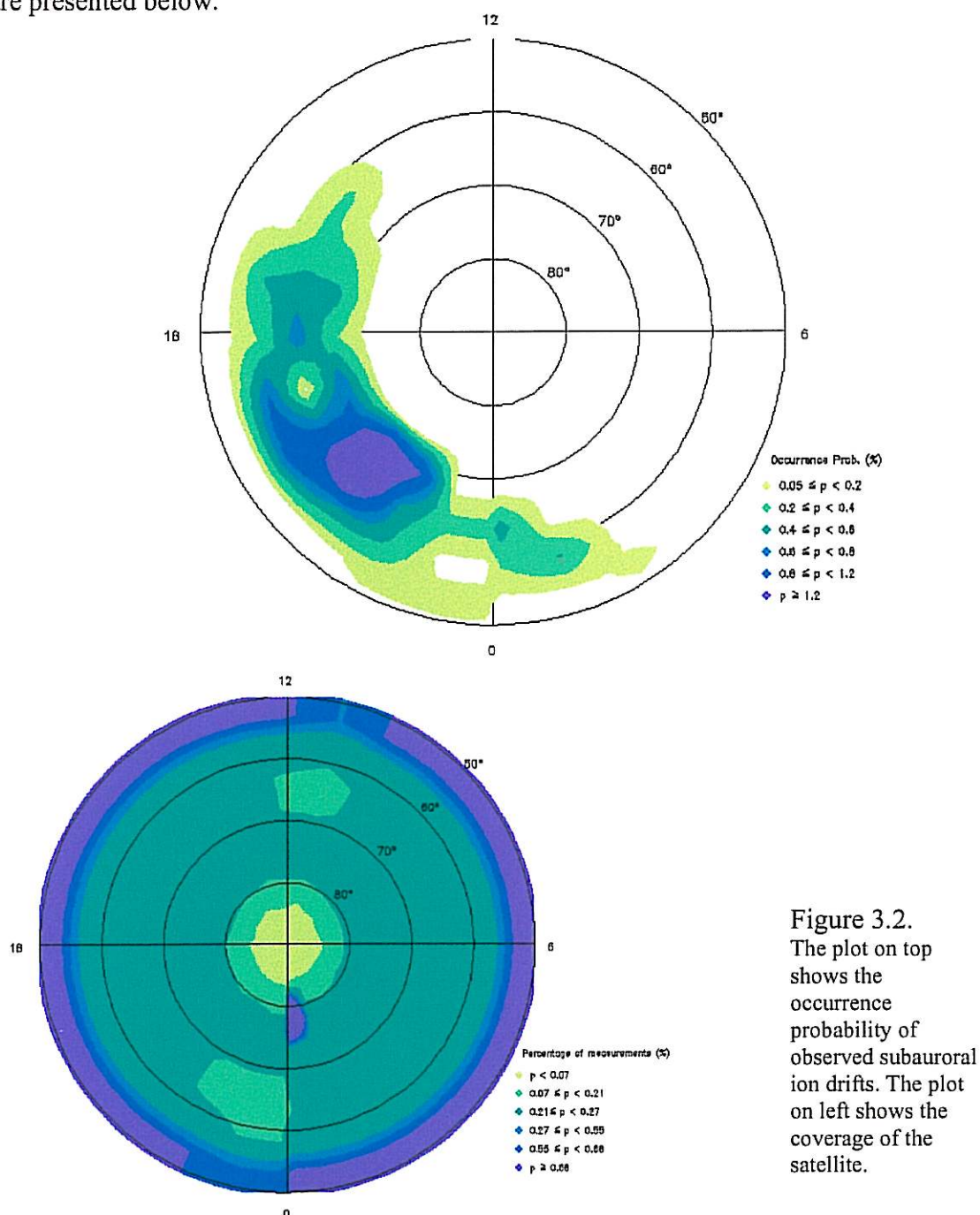


Figure 3.2.
The plot on top shows the occurrence probability of observed subauroral ion drifts. The plot on left shows the coverage of the satellite.

The plot shows that the distribution of SAID occurrence probability is concentrated to the premidnight sector and its maximum located in the 2000 to 2300 MLT region, with rather small probability before 1800 MLT and after 2400 MLT.

For each magnetic local time, the occurrence probability was also determined and its distribution is showed in Figure 3.3.

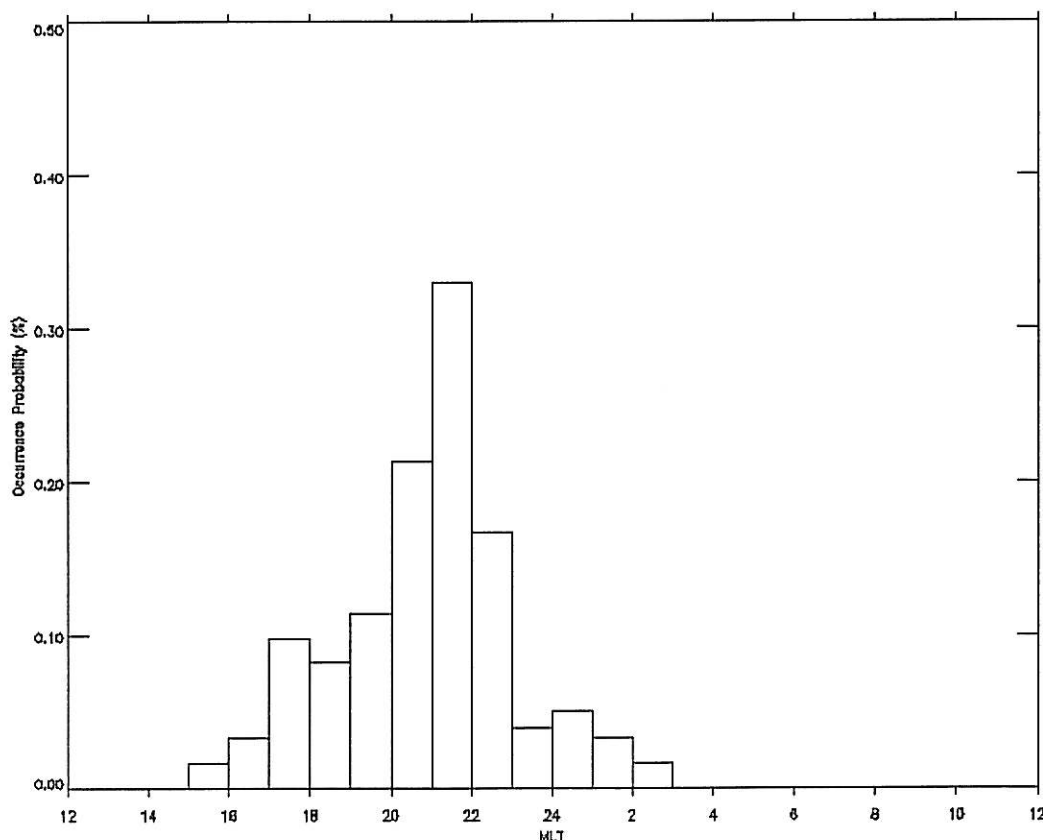


Figure 3.3.
Occurrence probability for each hour in magnetic local time.

The distribution profile seen on this plot confirms the results previously mentioned about Figure 3.2.

The intensity of the poleward electric field component of each SAID event was plotted in magnetic local time, and the result shows that the intensity of the subauroral ion drift is larger in the premidnight time region located between 2100 and 2300 MLT. In this region events with poleward electric field intensities greater than 400 mV/m (ion drift velocities greater than 13 000 m/s) were observed.

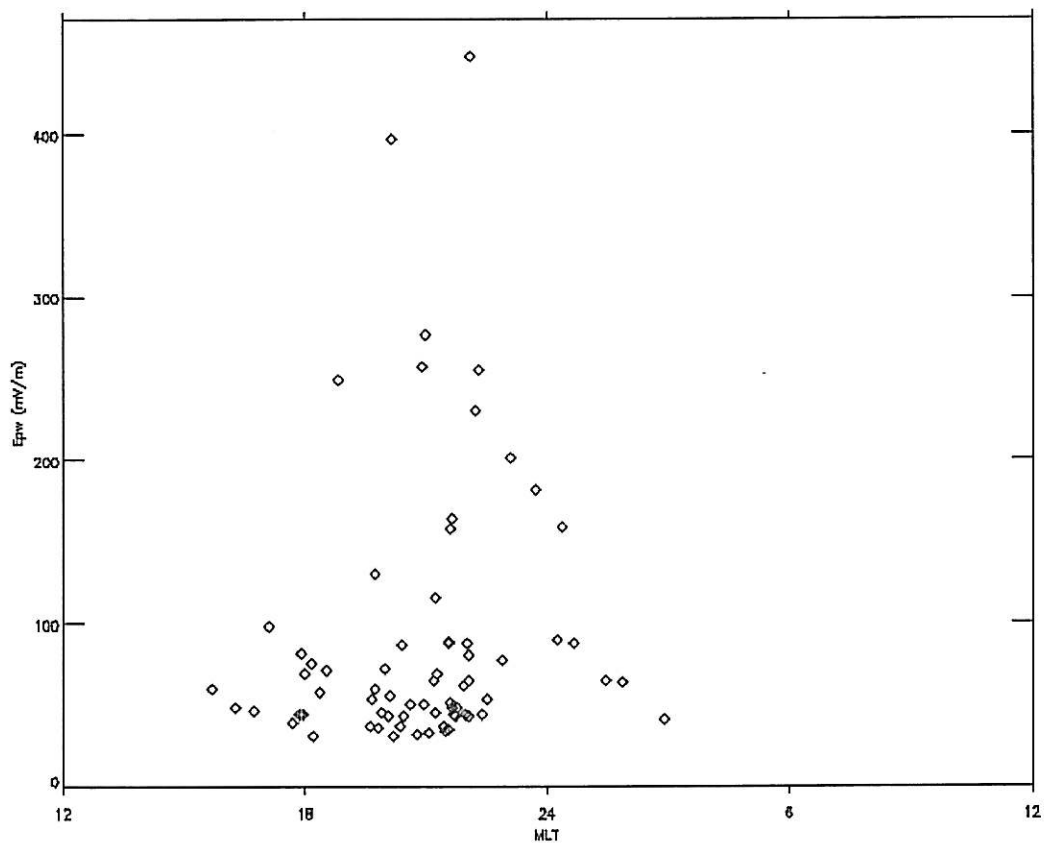


Figure 3.4.
Distribution of the maximum electric field poleward component versus magnetic local time.

This result might indicate one or both of the following:

- the midlatitude trough may have its deepest point in this region.
- the substorm-related currents may have a maximum in this region.

Defining the scale-size of a subauroral electric field structure as the full width at half maximum of the electric field peak (represented by W in Figure 3.1.) correspondent to the SAID event, the maximum electric field magnitude was plotted versus the scale-size of the subauroral electric field structure in Figure 3.5.

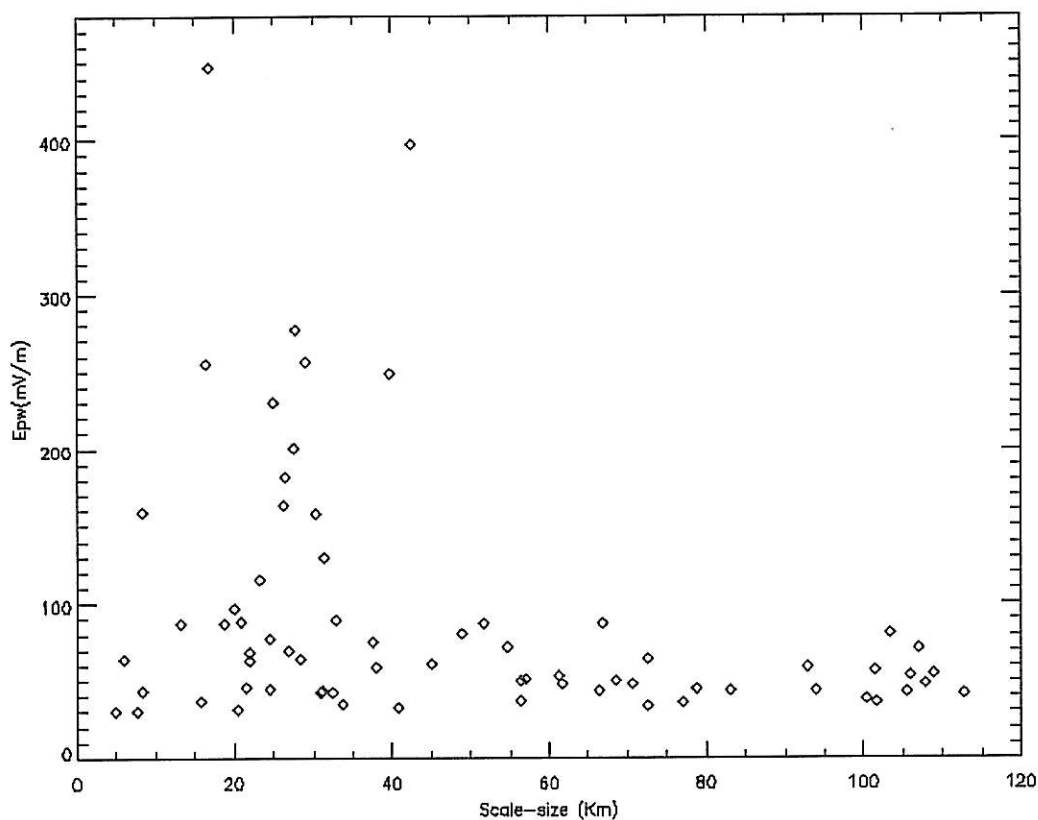


Figure 3.5.

Distribution of the maximum poleward electric field component versus the scale-size of the subauroral electric field structures.

It is seen that stronger electric fields have scale-sizes between 10 and 40 km, whereas weaker events have a larger spread in scale-size.

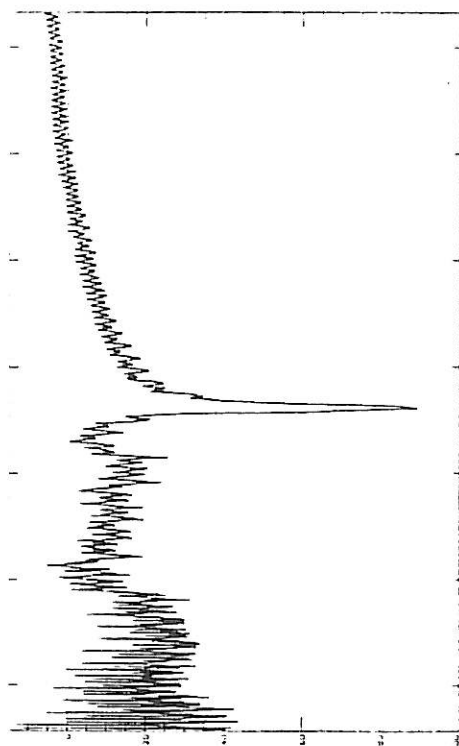
In order to study the relation existent between the occurrence of magnetospheric substorms and the generation of subauroral electric fields, an attempt was made to evaluate the interval of time existent between the start of the substorm expansion phase and the instant of the occurrence of each SAID event. For this evaluation the auroral electrojets indices were used, particularly the AL index³.

In Figure 3.6. it is shown one example of how this method was applied to two specific SAID events occurred on the same day.

³ These data was obtained from the *World data center for geomagnetism, Kyoto* web site: <http://swdcdh.kugi.kyoto-u.ac.jp/>

Astrid 2 data 1999 04 14 (DOY 104)

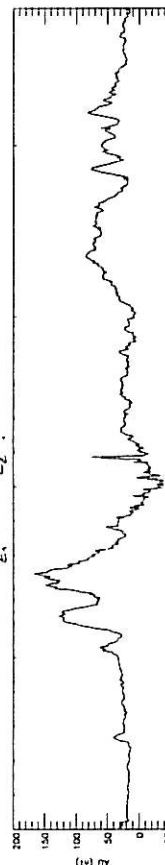
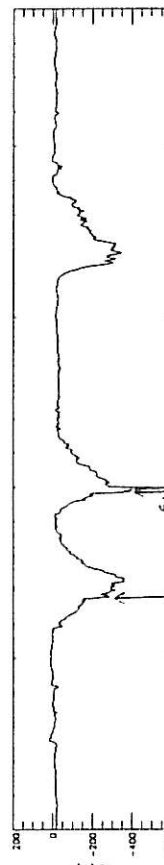
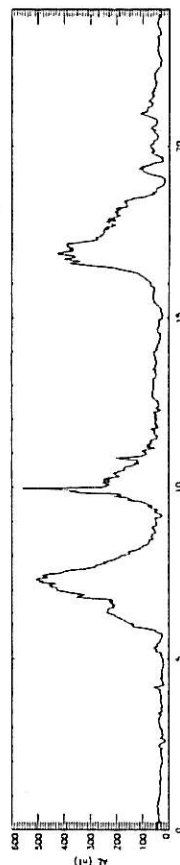
Orbit 14895 → E₁



UT
AUL
CALCUL
INT

07/27/02 07/28/02 07/29/02 08/01/02 08/02/02 08/03/02

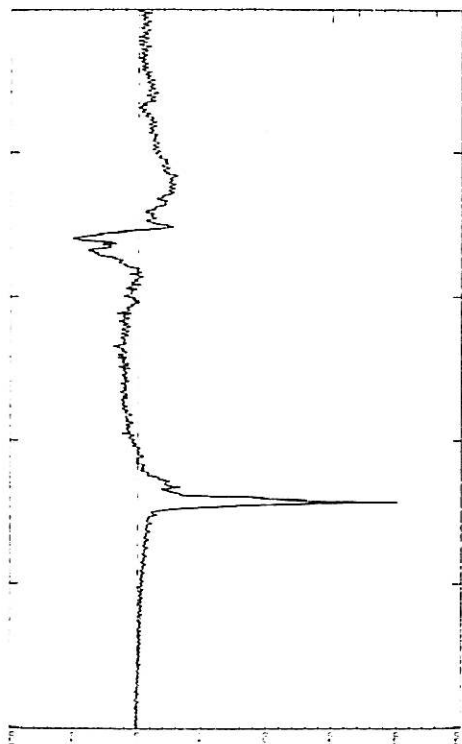
99.3 99.3 99.3 99.3 99.3 99.3
-1.1 107.24 107.24 107.24 107.24 107.24
00.00 00.00 00.00 00.00 00.00 00.00



Date: 19990414

Astrid 2 data 1999 04 14 (DOY 104)

Orbit 14900 → E₂



UT
AUL
CALCUL
INT

10/20/00 10/22/00 10/24/00 10/26/00
1000 1000 1010 1011
50.2 64.8 71.6 74.3
23.08 23.05 23.01 22.57

Figure 3.6.
Determination method of the interval of time from the start of the substorm expansion phase for two specific SAID events.

Analysing the AL index curve from the day of the events, a search for a rapid change in the slope of the curve was done. This breaking point was interpreted as the start of the substorm expansion phase.

This point is marked in the curve as S_1 and S_2 for the events E_1 and E_2 respectively. Therefore, the interval of time, Δt_i , correspondent to the event i , will be defined as $\Delta t_i = E_i - S_i$.

Figure 3.7. shows the plot of the magnitude of the poleward electric field component versus the determined interval of time Δt , for each SAID event.

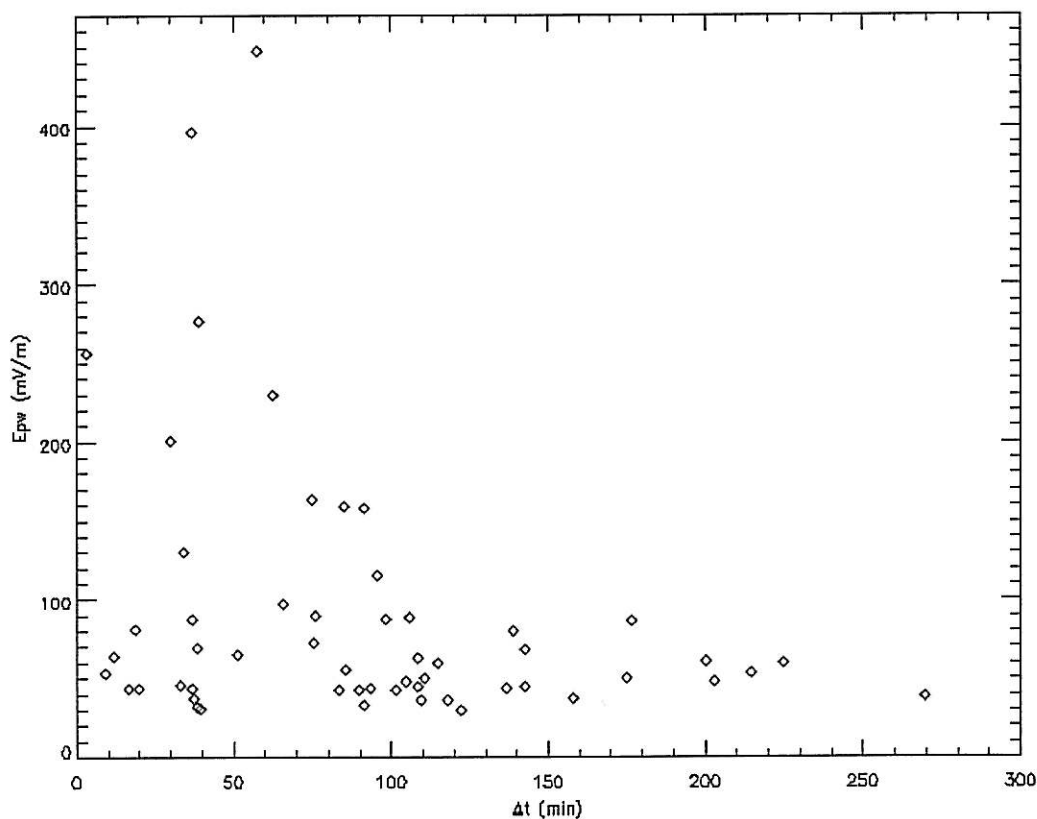


Figure 3.7.

Distribution of the electric field poleward component versus interval of time from the start of the expansion phase.

Large subauroral ion drifts are observed between 30 to 80 minutes after the start of the substorm expansion phase.

To study the annual variation of the subauroral electric field strength, the magnitude of the poleward component was plotted versus day of year (DOY) and it is shown in Figure 3.11.

To make the analysis easier, the DOY corresponding to events from the Southern Hemisphere was shifted 182 days. The colour code used in the first panel shows the dependence on the geomagnetic activity index Kp .

In second panel a colour code was used to give information about the coverage of the satellite. Each colour refers to the position of the satellite within one specific

MLT-region, as indicated by the legend. This coverage study was done dividing the entire operational period of Astrid-2 in intervals of five minutes, plotting for each interval the correspondent colour coded trace.

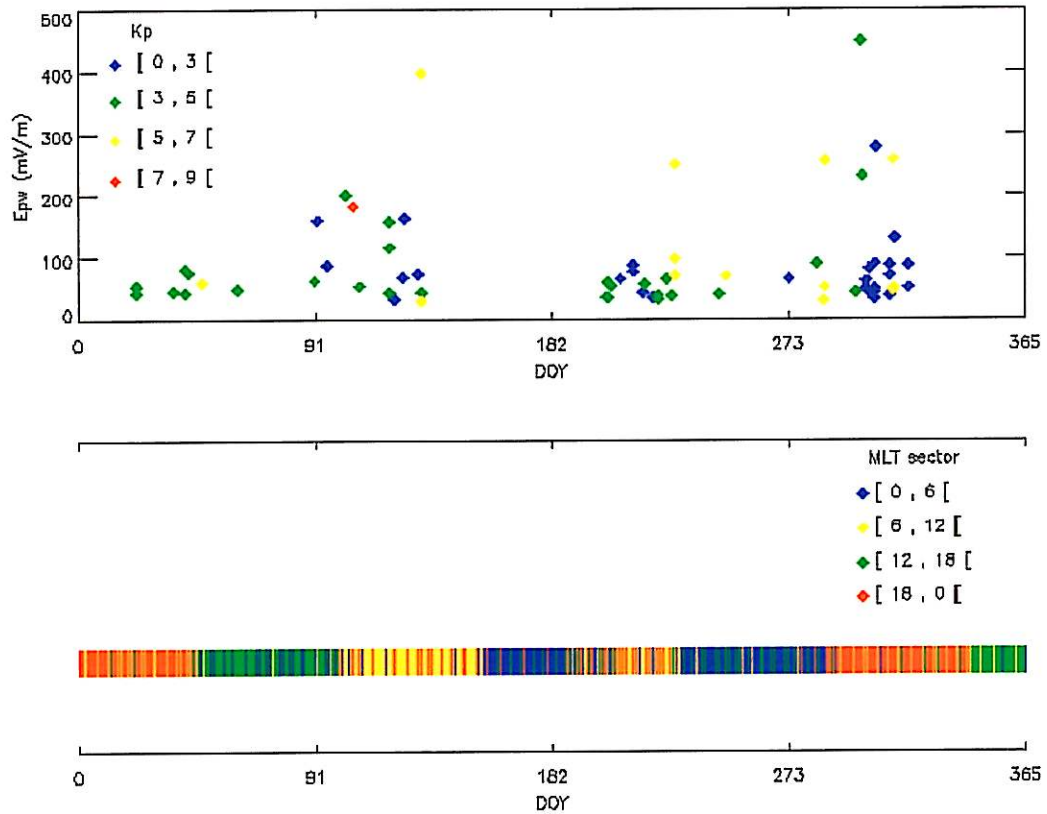


Figure 3.8.

Distribution of the poleward component of the electric field versus day of year. The colour code in the first panel shows the magnetic activity as given by the Kp index. In the second panel information on the coverage of Astrid-2 is given.

In the first half of the year strong electric fields are observed around DOY 100, while for the second half, a concentration of intense events are seen close to DOY 300. Both distribution peaks occur slightly after the equinoxes, and any events are detected during solstices.

The coverage information shows us that on the period around Summer solstice (DOY 172) the satellite was most of the time measuring on the posmidnight sector, while for the period around winter solstice (DOY 355) it was on the afternoon sector. The fact that during these periods of the year, the orbit of the satellite was crossing MLT sectors where the occurrence probability of a SAID event is low (see Figure 3.2.), means that we cannot draw any conclusions on the fact that no SAID events are observed.

The appearance of intense electric fields doesn't seem to have a significant activity dependence, since the SAEF events with magnitudes greater than 150 mV/m are distributed quite homogeneously over the Kp range. However, the two intense events

whose location in time deviates from the distribution peaks, occurred at conditions of high activity.

The increase in magnetic activity during the equinox periods, as well as the decrease in ambient conductivity during Winter solstice, are two important factors that may lead to the creation of intense electric fields. In this way, it is expected that more SAID events are detected and have larger magnitudes, during the period of the year where both factors are set in with an appropriate balance between them.

This seems to occur during the autumn season, where, in fact, we can find a high concentration of events, some of them having rather high magnitudes.

In Figure 3.9. the corrected geomagnetic latitude of the SAID events is plotted versus magnetic local time. A colour code is used once more to distinguish between different activity levels.

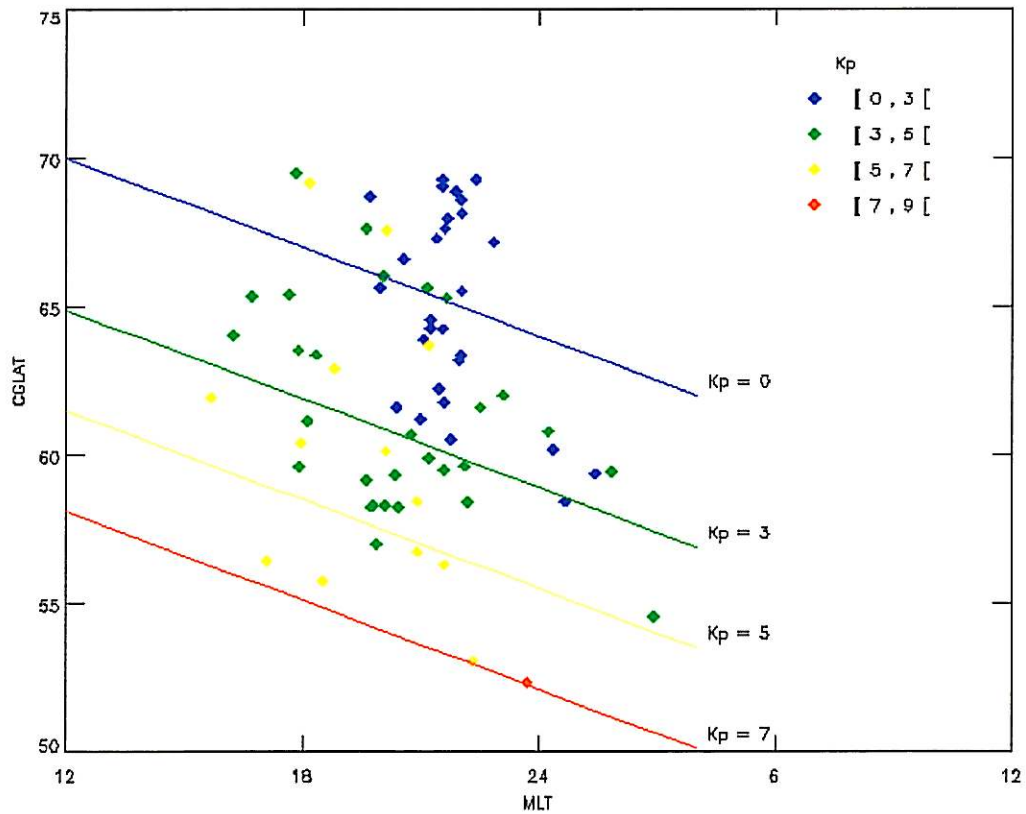


Figure 3.9.

Plot of the corrected geomagnetic latitude of the SAID events versus magnetic local time. The events are colour coded according to Kp values for the time of observations. Also represented is the position of the midlatitude trough minimum for different magnetic activity levels.

Also represented is the position of the midlatitude trough minimum for different values of Kp , according to the relation obtained by *Best et al.*[1984] and quoted below

$$\text{Inv.lat. (trough min)} = 64.0^\circ - 1.7Kp - 0.5t \quad (3.1.)$$

where t is local time with respect to midnight.

A tendency of the SAID occurrence moving towards lower latitudes with increasing magnetic activity, seems to exist. However, this movement does not follow exactly the movement of the trough, as defined by the relation presented above.

A majority of the events occur poleward of the midlatitude trough. To study if the relative location of SAID and trough depends on the electric field peak magnitude, a plot for each activity level was done, where the coloured symbols stands for the events collocated with the trough, whereas the dark symbols mark events located poleward of the trough. These plots are shown on Figure 3.10.

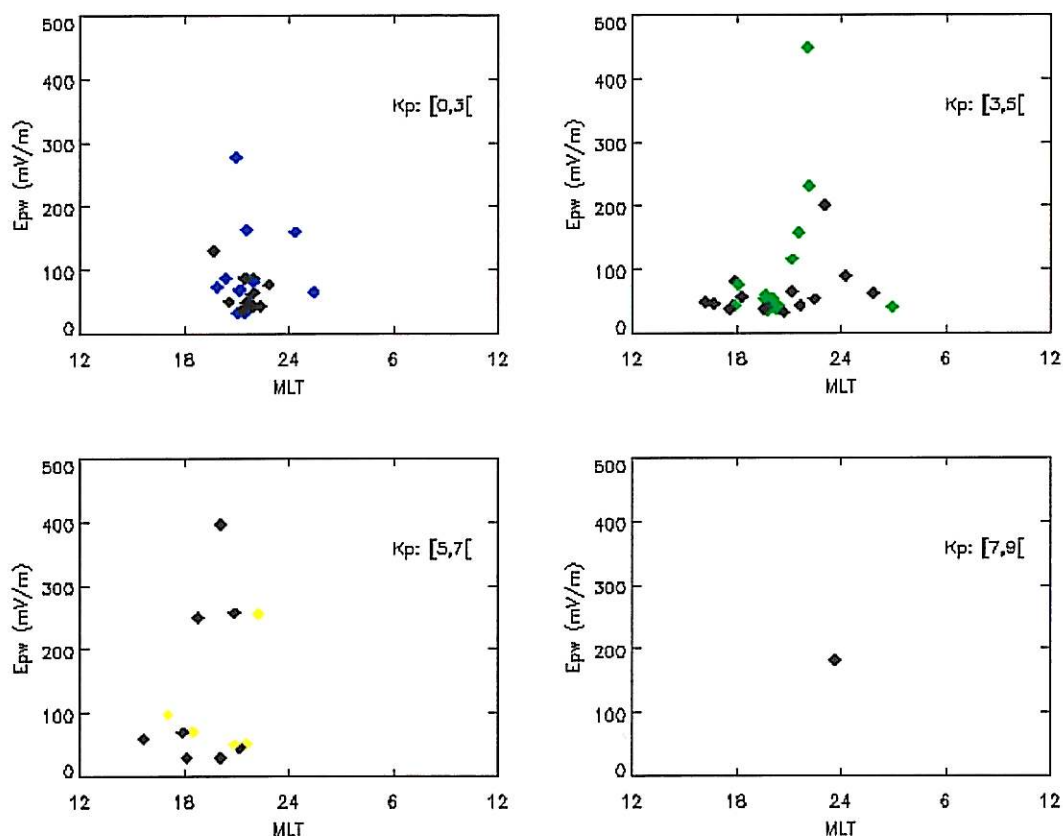
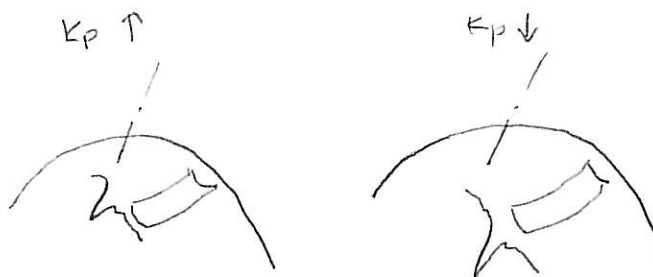


Figure 3.10.

Plot of SAID magnitude versus MLT according to magnetic activity level. The dark symbols refer to events located poleward to the trough.

For low activity levels, intense events occur collocated with the midlatitude trough. Under conditions of high activity, strong events seem to occur poleward of the trough. However, these conclusions are not supported by a good statistics, since there isn't a uniform distribution of events through the different activity levels.



The IMF By dependence for SAID events was studied using data from the WIND satellite⁴. For the events where IMF data were available, the corresponding electric field magnitude was plotted versus IMF By.

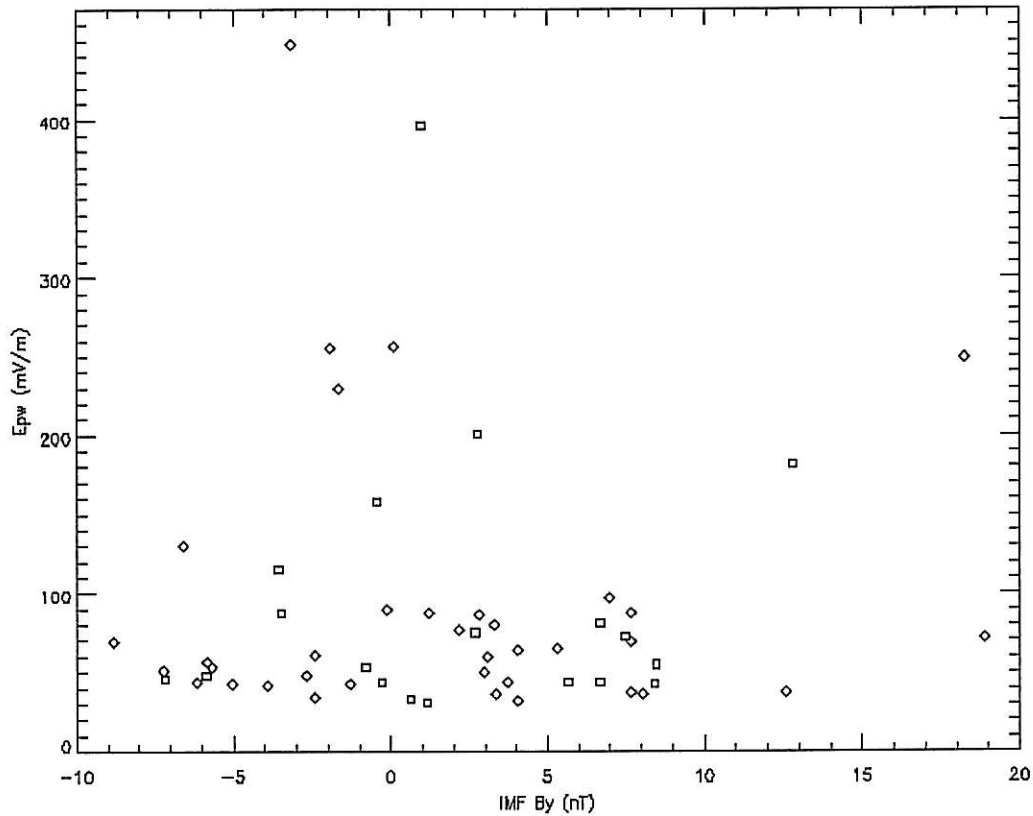


Figure 3.11.
Distribution of the magnitude of SAID events versus the y component of the interplanetary magnetic field.

In order to find the correspondent IMF By value to each SAEF event, one had to take into account the fact that the measurements made by the Wind satellite were not done at the same position where the events were detected by Astrid-2.

In this way, knowing the instant of the SAEF event, t_{Astrid} , a search was done in order to find the instant t_{Wind} , such that

$$t_{Wind} + t_{prop} = t_{Astrid} \quad (3.2.)$$

where t_{prop} stands for the time of propagation of the IMF, transported by the solar wind, from the position where it was measured until the position where the SAEF event occurred. This was calculated considering the position of the Wind satellite, and the x-component of the velocity of the solar wind, at the instant t_{Wind} .⁵

⁴ Available on the web page from the National geophysical data center: www.ngdc.noaa.gov/stp/

⁵ Here is neglected the distance of the Astrid-2 satellite relatively to the Earth (center of the reference system) in comparison with the distance of the Wind satellite.

$$t_{\text{prop}} = \frac{x_{\text{Wind}}(t_{\text{Wind}})}{v_{\text{sw}}(t_{\text{Wind}})} \quad (3.3.)$$

As we can see, the time of propagation is a function of t_{Wind} .

So, the IMF B_y value considered to correspond to each event, was the one measured at the instant t_{Wind} such that, the difference between $t_{\text{Wind}} + t_{\text{prop}}(t_{\text{Wind}})$ and t_{Astrid} is minimal.

The results show that the strongest fields detected on the Northern Hemisphere correspond to positive B_y , whereas for the Southern Hemisphere the strongest fields (magnitude greater than 100 mV/m) seem to occur when B_y assume negative values, exception made to one event occurring for $B_y \approx 18$ nT.

3.2. Case Study Results

After a global overview of the available data has been made, a more detailed study was done for some selected orbits.

From the set of 72 SAID events, 5 were selected. All of them show a clear poleward electric field peak, with a magnitude between 70 and 400 mV/m.

Based on the magnetic field data, a calculation of the field aligned currents (FAC) and of the height integrated Pedersen conductivity was done, for each selected orbit.

Using the Maxwell equation

$$\nabla \times \vec{B} = \mu_0 \vec{j} + \frac{1}{c^2} \frac{\partial \vec{E}}{\partial t} \quad (3.4.)$$

and neglecting electric field oscillations on time-scales shorter than the time it takes Astrid-2 to pass the SAID event, as well as the presence of an isotropic medium, results for the field aligned component of the current (at ionospheric altitudes can be considered as being vertical) the following expression

$$j_z = -\frac{1}{\mu_0} \frac{\partial B_x}{\partial y} \quad (3.5.)$$

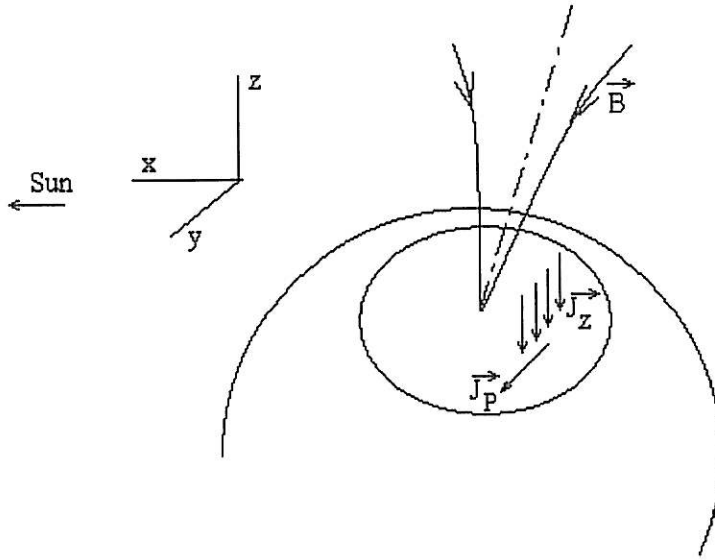


Figure 3.12.
Schematic representation of the field-aligned and Pedersen currents.

It was also considered B_y to be uniform in the x-direction $\left(\frac{\partial B_y}{\partial x} = 0\right)$.

The height integrated Pedersen current in a given point is obtained by integrating the FAC that is arriving to and closing through the ionosphere.

$$J_P(y_1) = \int_{y_0}^{y_1} j_z dy = \int_{y_0}^{y_1} -\frac{1}{\mu_0} \frac{\partial B_x}{\partial y} dy \quad (3.6.)$$

Knowing the y-component of the ionospheric electric field, the height integrated Pedersen conductivity can be calculated by

$$\Sigma_P = \frac{J_P}{E_y} \quad (3.7.)$$

Thus we can calculate J_P and Σ_P for each measurement point i by using the following formulation

$$J_z(i) = -\frac{1}{\mu_0} \frac{B_{2mee}(i) - B_{2mee}(i-1)}{y(i) - y(i-1)}$$

$$J_P(i) = -\frac{1}{\mu_0} (B_{2mee}(i) - B_{2mee}(0)) \quad \text{and} \quad \Sigma_P(i) = \frac{J_P(i)}{E_{3mee}(i)} \quad (3.8.)$$

In the next pages is shown all the information collected for each of the five selected orbits.

It is presented the available data from Astrid-2 measurements:

1. E2mee – x-component of the electric field.
2. E3mee – y-component of the electric field.
3. B2mee – x-component of the magnetic field.
4. B3mee – y-component of the magnetic field.
5. N2 – electron density.
6. VFG1234 – floating ground potential.

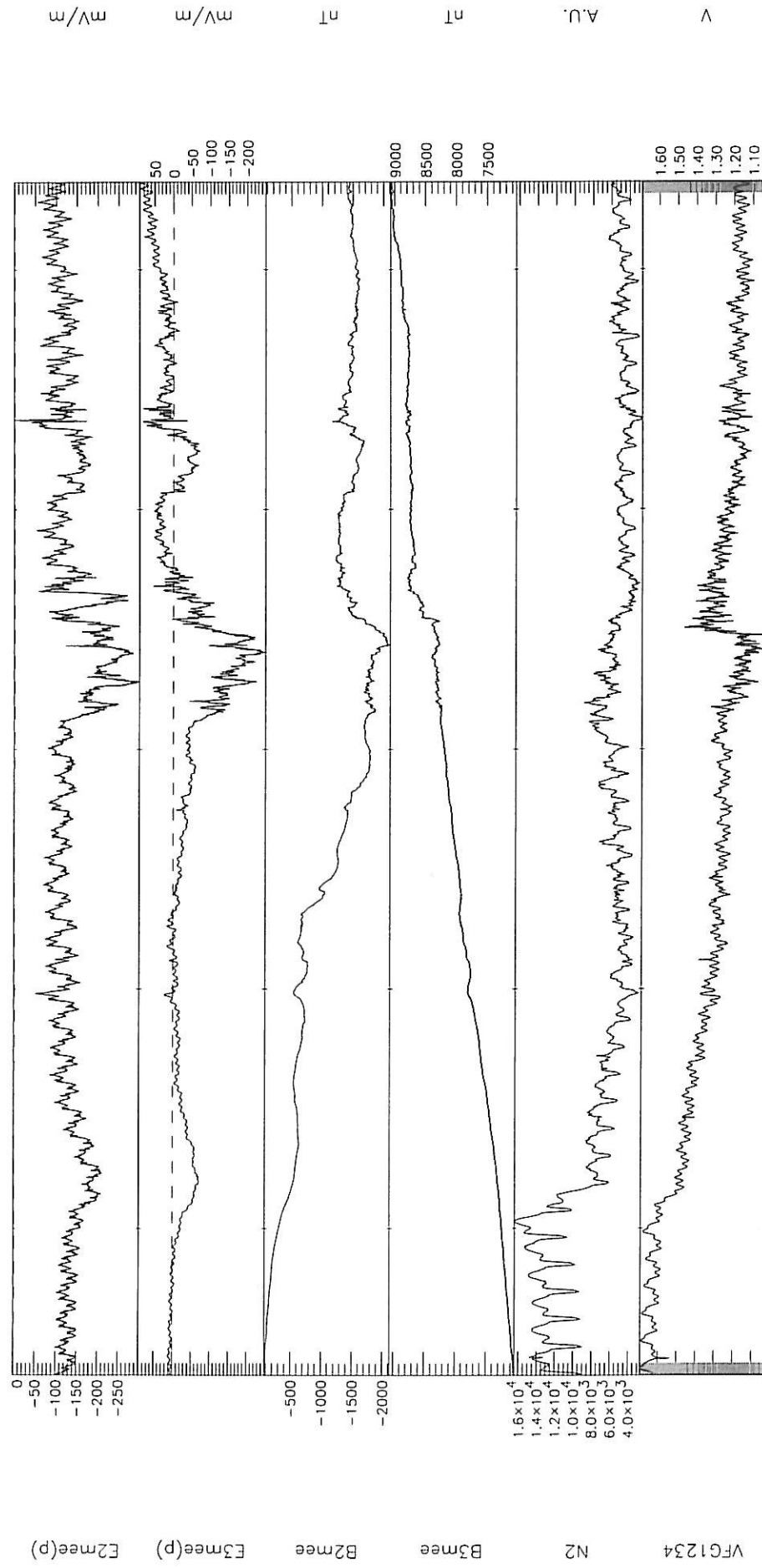
and also the profiles obtained from the calculations described above:

7. Symbolic representation of the intensity and direction of the FAC.
(red colour indicates downward current; blue colour indicates upward colour). Simultaneously is shown again the E3mee curve.
8. j_z – Field aligned current.
9. J_p – Height integrated Pedersen current.
10. Σ_p – Height integrated Pedersen conductivity.

With respect to plot 7, a comparison of the symbolic representation of the FAC intensity between the different selected events, should not be done, since it corresponds to different scales. For magnitude analysis, plot 8 should be taken into account.

Astrid-2 data 1999-02-18 (DOY 49)

Orbit 11882



UT	08:49:00	08:50:00	08:51:00	08:52:00	08:53:00
Alt	1025	1026	1026	1027	1027
CGLat	-55.1	-58.4	-61.6	-64.8	-68.0
MLT	18:30	18:37	18:46	18:56	19:10

Orbit = 11882

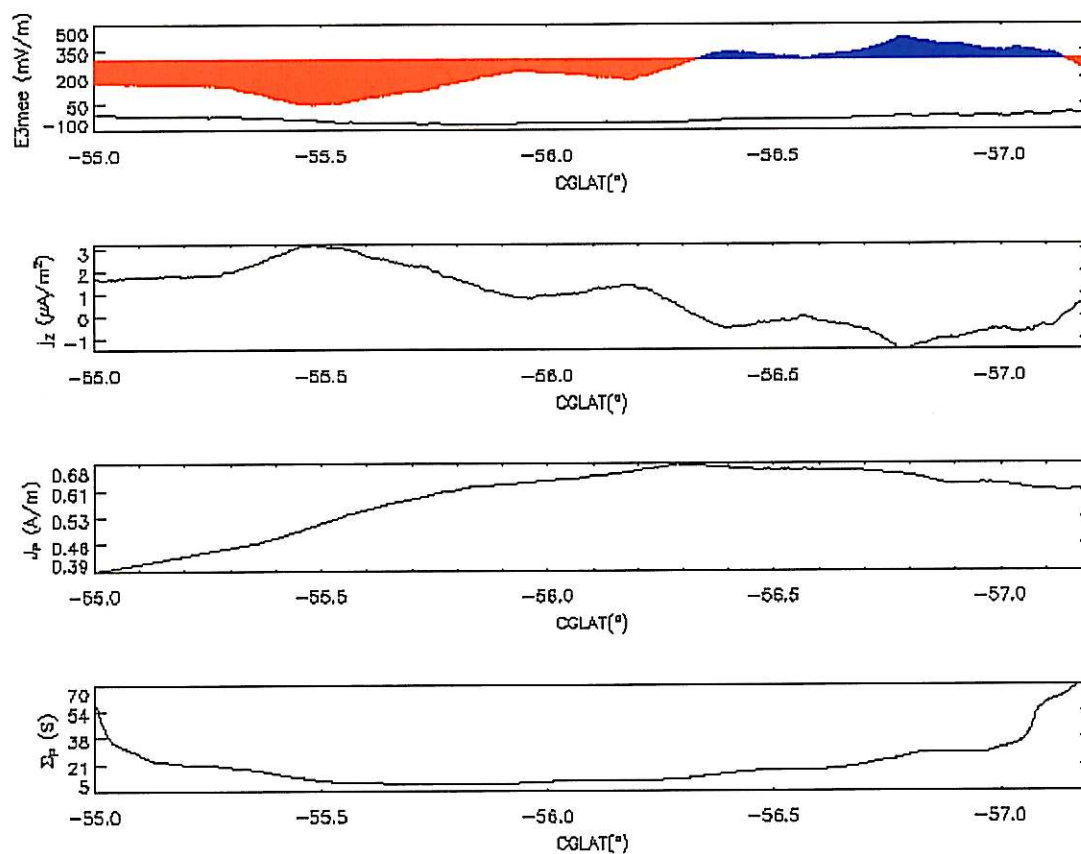


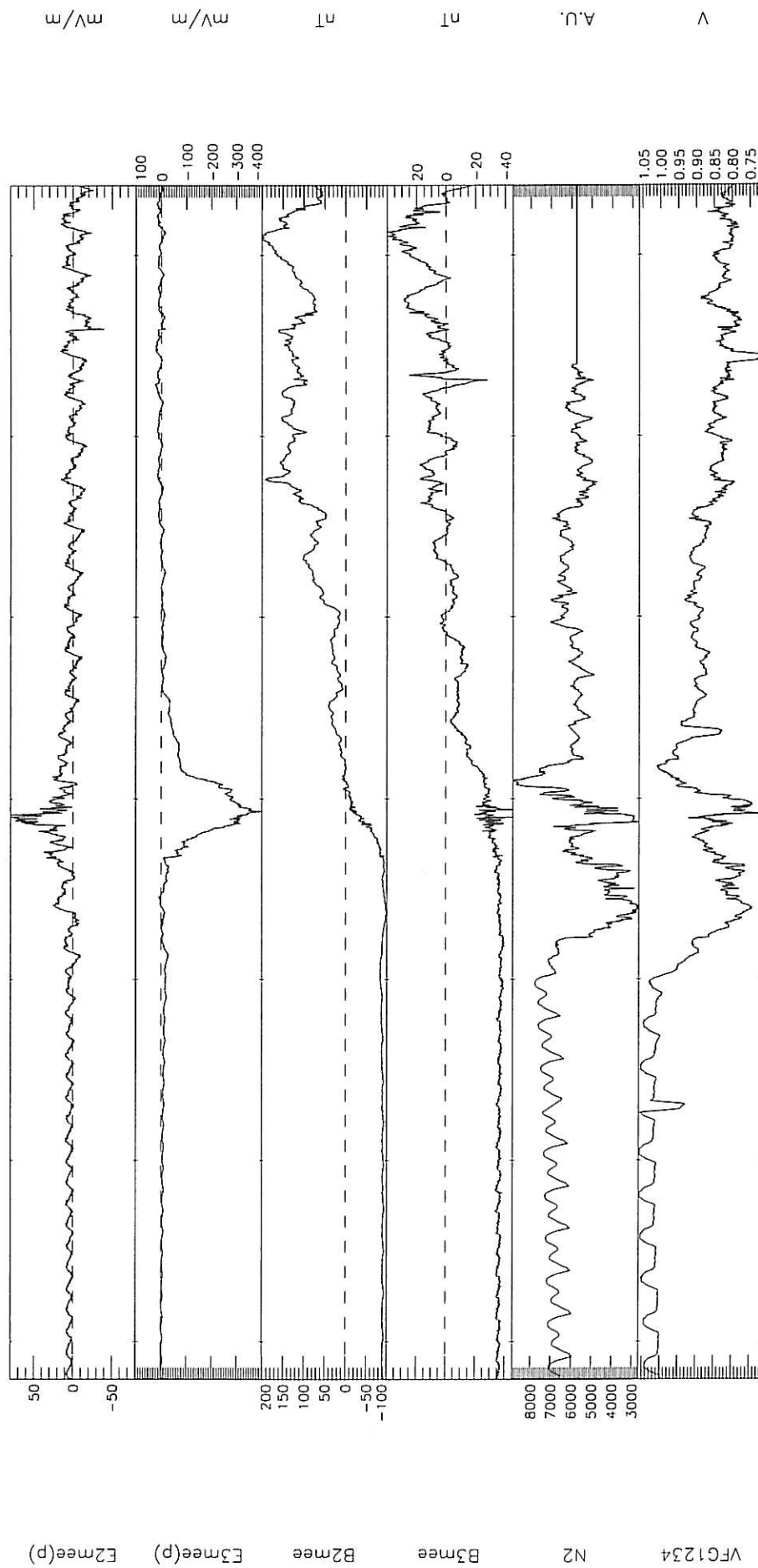
Figure 3.14.
Plots 7, 8, 9 and 10 correspondent to orbit 11882

Orbit 11882	18-02-1999
Kp	6.7
Scale-size	0.40 ₋₋₋

Table 3.1.
Some additional case information

Astrid-2 data 1999-05-13 (DOY 133)

Orbit 16476



UT	04:19:30	04:20:00	04:20:30	04:21:00	04:21:30	04:22:00	04:22:30
Alt	1014	1014	1013	1013	1012	1012	1011
CGLat	55.4	57.0	58.6	60.2	61.7	63.3	64.9
MLT	20:07	20:07	20:08	20:08	20:08	20:09	20:09

Orbit = 16476

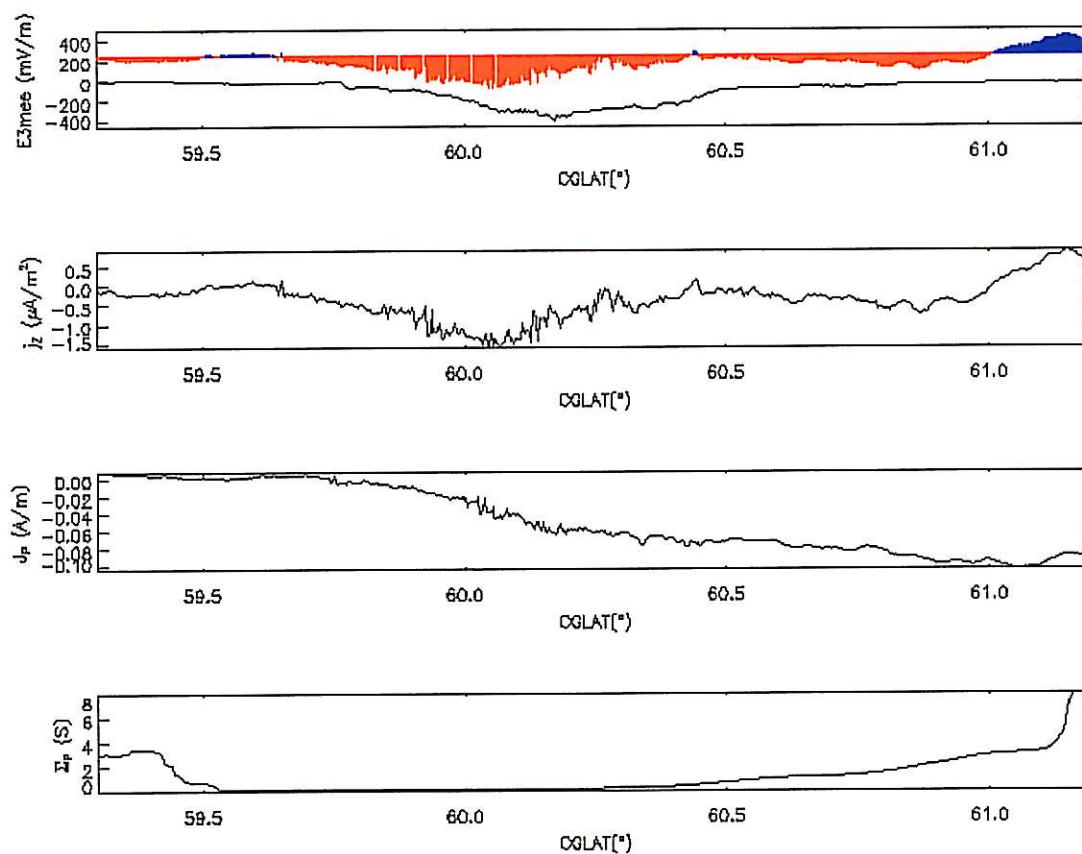


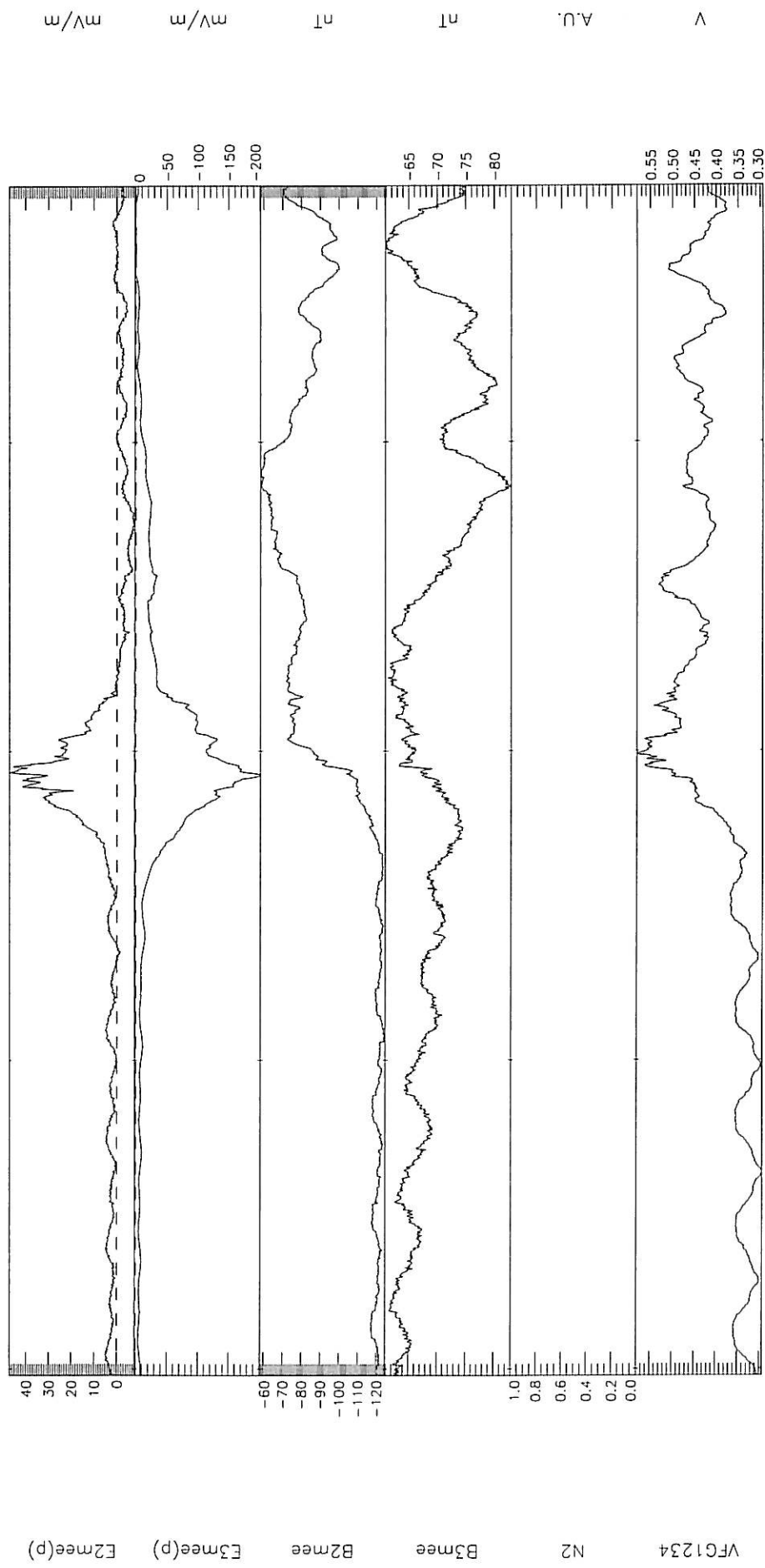
Figure 3.16.
Plots 7, 8, 9 and 10 correspondent to orbit 16476

Orbit 16476	13-05-1999
Kp	5
Scale-size	0.42 ^o

Table 3.2.
Some additional case information

Astrid-2 data 1999-04-14 (DOY 104)

Orbit 14900



UT	10:20:30	10:20:50	10:21:10	10:21:30
Alt	1009	1009	1009	1009
CGLat	59.9	61.0	62.1	63.2
MLT	23:07	23:07	23:06	23:06

Orbit = 14900

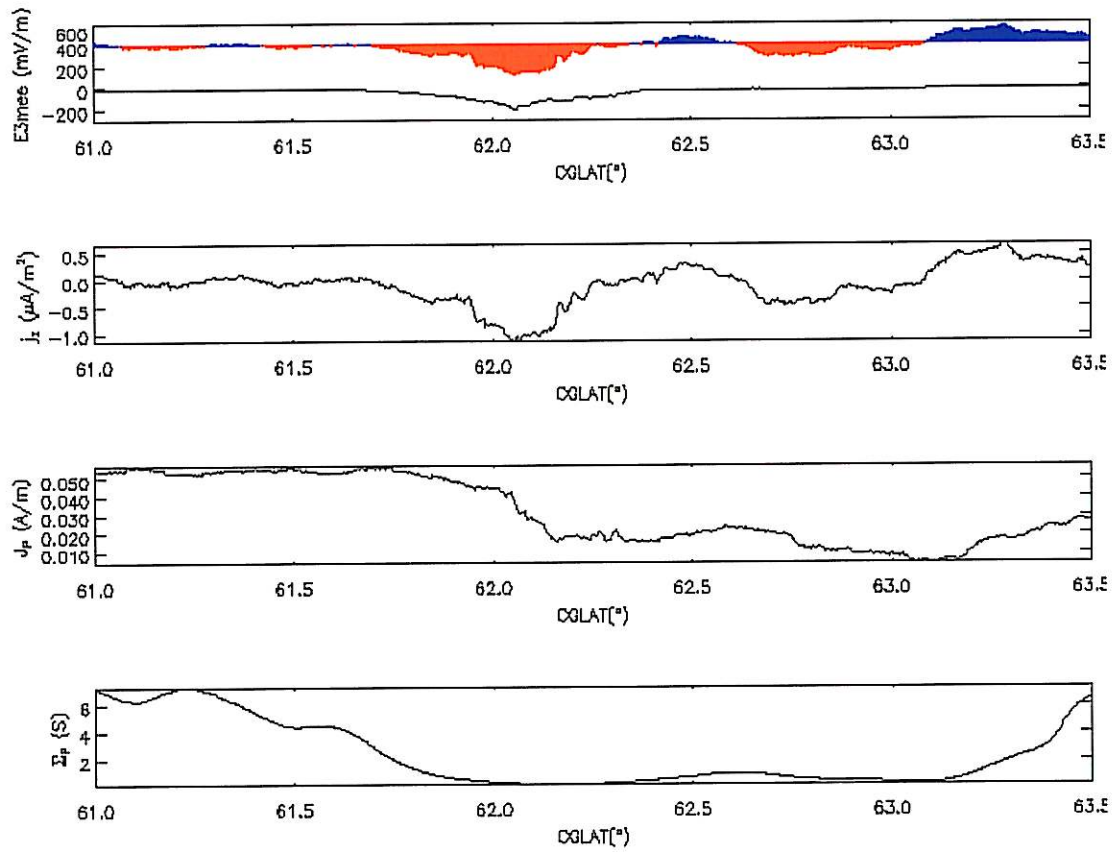


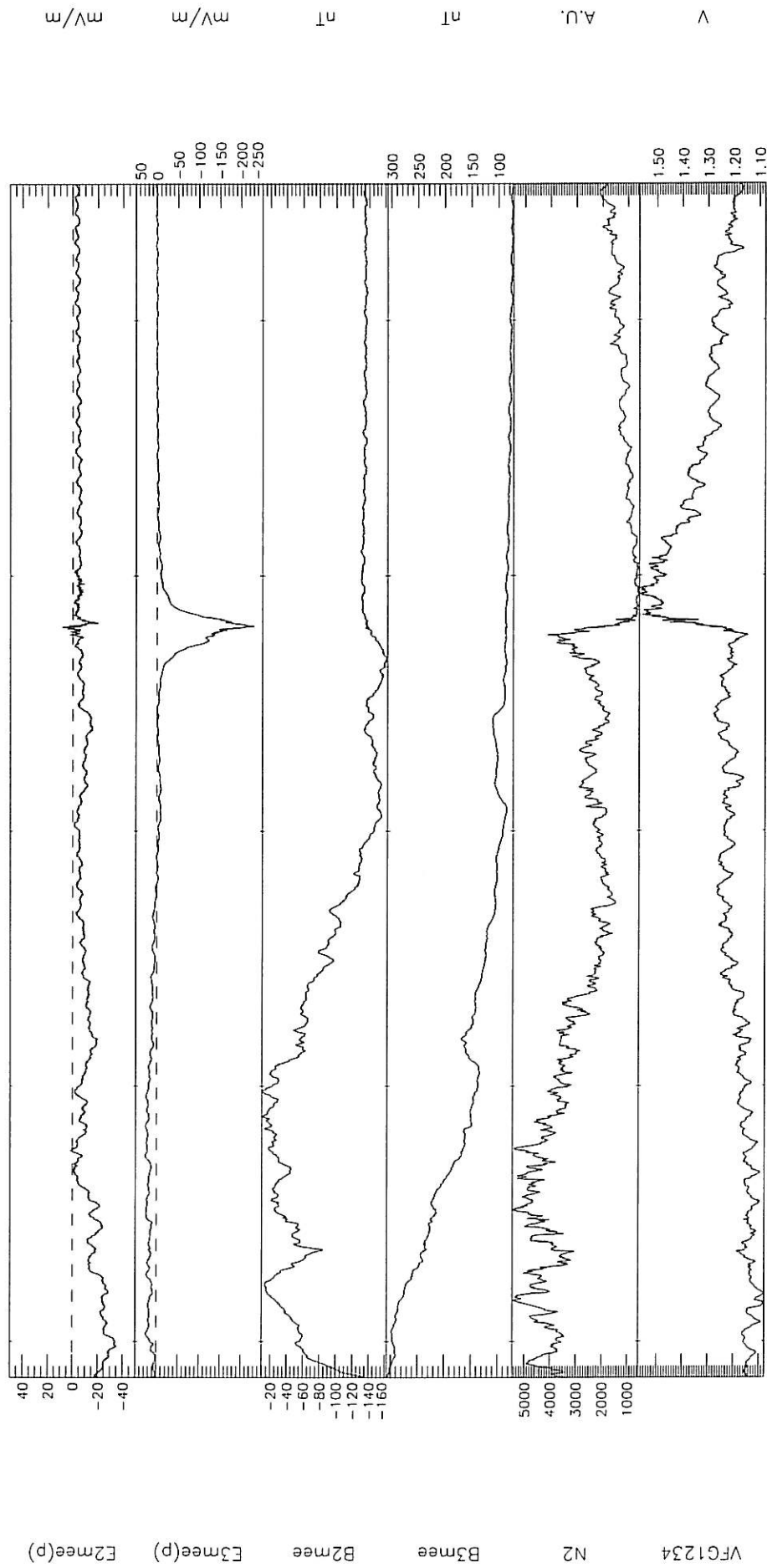
Figure 3.18.
Plots 7, 8, 9 and 10 correspondent to orbit 14900

Orbit 14900	14-04-1999
Kp	3
Scale-size	0.28 ^c

Table 3.3.
Some additional case information

Astrid-2 data 1999-05-01 (DOY 121)

Orbit 15827



UT	08:04:00	08:05:00	08:06:00	08:07:00	08:08:00
Alt	1001	1002	1002	1003	1004
CGLat	-67.1	-64.1	-61.0	-57.9	-54.8
MLT	22:37	22:27	22:18	22:11	22:05

Orbit = 15827

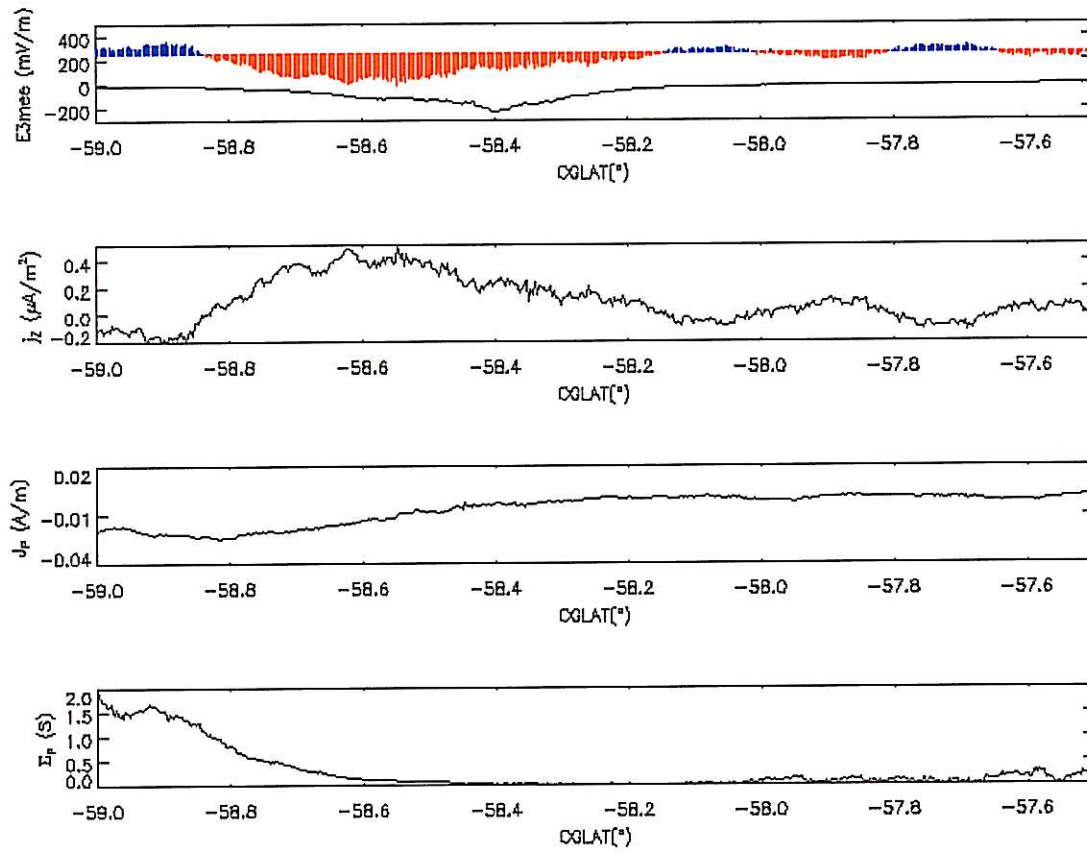


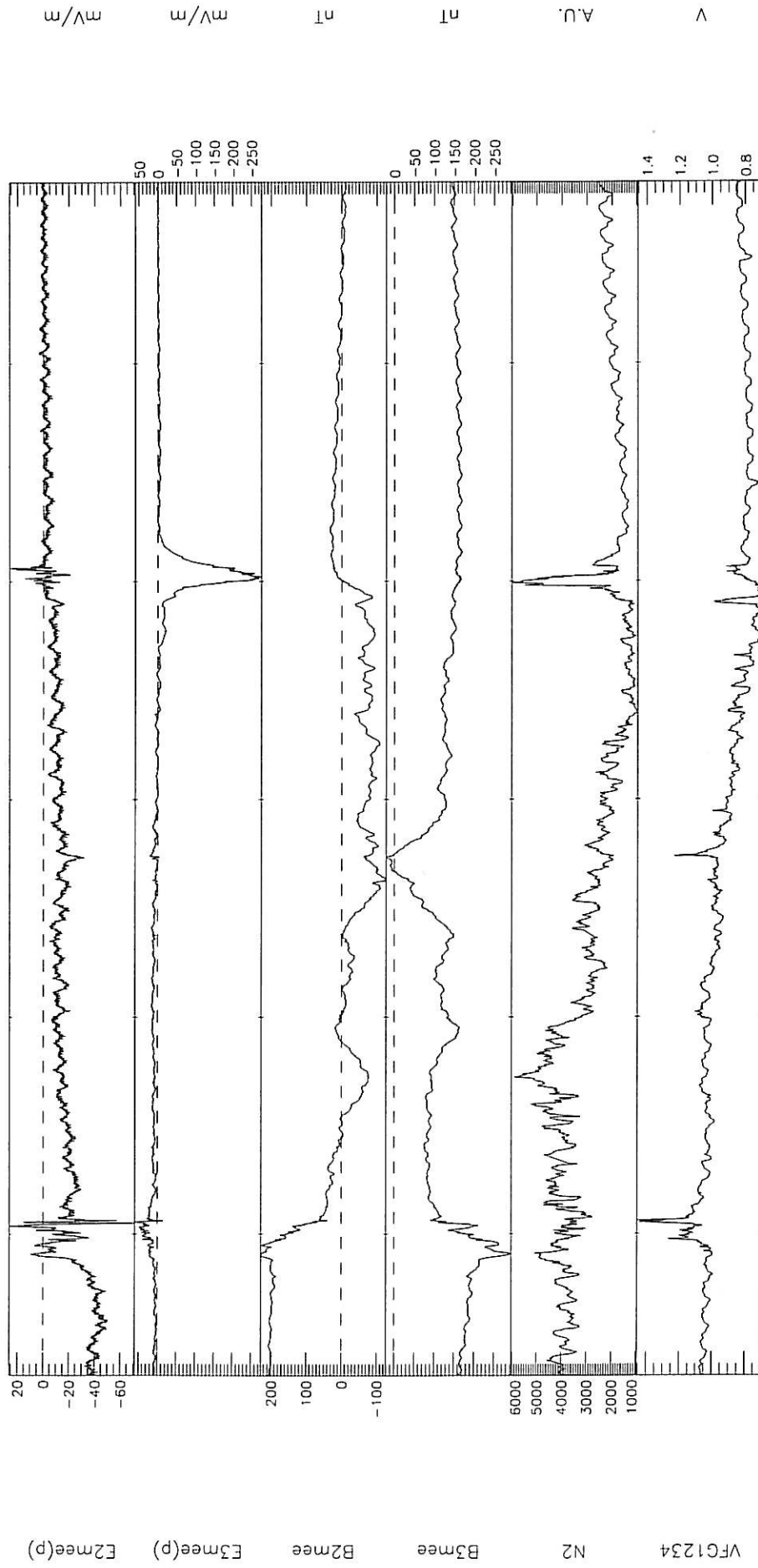
Figure 3.20.
Plots 7, 8, 9 and 10 correspondent to orbit 15827

Orbit 15827	01-05-1999
Kp	2.7
Scale-size	0.25 c

Table 3.4.
Some additional case information

Astrid-2 data 1999-05-07 (DOY 127)

Orbit 16143



UT	02:20:00	02:21:00	02:22:00	02:23:00	02:24:00
Alt	1001	1001	1002	1003	1004
CGLat	-70.7	-67.6	-64.5	-61.3	-58.2
MLT	20:58	20:59	20:59	20:60	20:60

Orbit = 16143

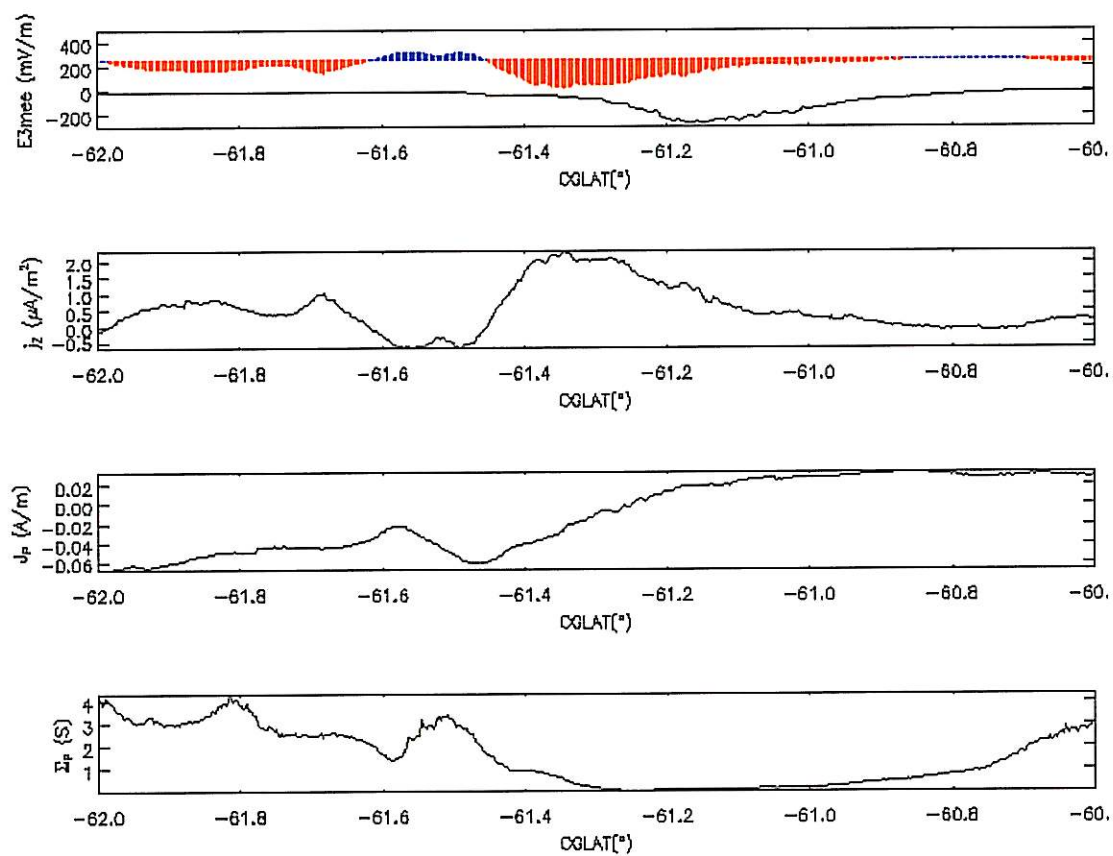


Figure 3.22.
Plots 7, 8, 9 and 10 correspondent to orbit 16143

Orbit 16143	07-05-1999
Kp	2.7
Scale-size	0.28°

Table 3.5.
Some additional case information



4. Discussion and Conclusions

From the study presented, a summary with the main results may be written.

- The occurrence probability of a SAID is higher in the MLT region located between 1900 and 2300, and between 60° and 70° CGLat.
- The stronger SAID events, with magnitudes between 100 and 450 mV/m, are concentrated in this MLT region.
- Stronger SAID events have rather small scale-sizes, whereas weaker events have a larger spread in scale-size.
- Strong SAID events occur 30 to 80 minutes after the start of the substorm expansion phase.
- SAID occurrence probabilities are peaked slightly after the equinoxes, with more and stronger events during the autumn season.
- The occurrence of SAID events does not show a strong magnetic activity dependence.
- The location of SAID events moves towards lower latitudes with increasing magnetic activity. The trough minimum shows a similar behaviour. However, the strongest SAID events seem to occur poleward of the trough minimum when the magnetic activity level is high, and collocated with the trough when magnetic activity is weaker.
- The strongest events detected on the Northern hemisphere occurred for positive IMF By, whereas for the Southern hemisphere they occurred for negative IMF By.
- The conductivity study shows that a SAID event corresponds to a conductivity reduction. However, the position of the conductivity minimum is not always collocated with the electric field peak:
 - On orbits 11882 and 16476, the SAID occurs polewards of the conductivity minimum. These events occurred for high magnetic activity.
 - On orbits 14900, 15827 and 16143, the SAID appears collocated with the conductivity minimum. These events occurred for lower magnetic activity.

The predominant location of SAID occurrence in the pre-midnight sector, shown in Figures 3.2. and 3.3., is in agreement with findings reported by *Spiro et al.* [1979], *Anderson et al.* [1991] and *Karlsson et al.* [1998b].

Keyser et al. [1998] proposed a physical mechanism that explains the formation and evolution of SAID in the course of a substorm. In this model a SAID is considered as the ionospheric signature of a magnetospheric interface between the cold plasmatrough and hot injected plasma moving inward. From this modelling results were obtained explaining why the SAID occurrence is predominant in the pre-midnight sector.

According to this study, a SAID is formed as a consequence of the azimuthal shear flow between the injected plasma and the partially corotating plasma trough in the vicinity of the plasmopause, and also as a consequence of the thermoelectric effects at

the interface. As a result from the relative direction of motion between the injected plasma and the plasmaspheric corotation (see Figure 4.1. below) the shear velocity at the interface is largest in the pre-midnight sector. Consequently, this model predicts the SAID occurrence to be predominant in this time sector.

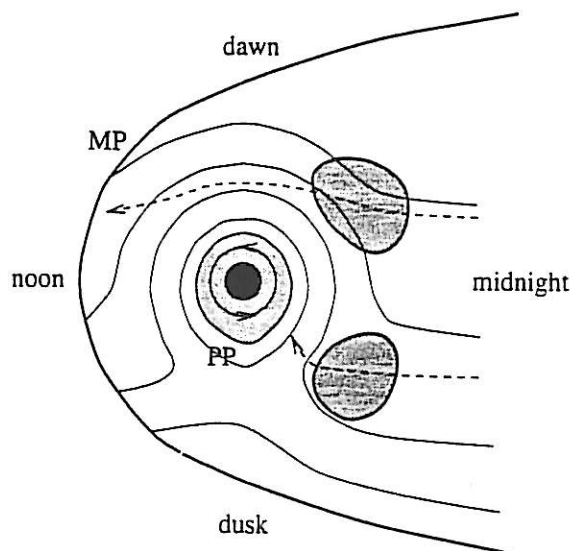


Figure 4.1.
Motion of the injected plasma front
through the magnetosphere.
(From Keyser, 1999)

However, in the study presented by Keyser *et al.* [1998] no reference is made to the relative location between SAID events and the midlatitude trough.

In one previous study reported by Anderson *et al.* [1993], a different production model of SAID events was presented. According to this model, subauroral field-aligned currents close via Pedersen currents with the outward flowing region-1 currents. These Pedersen currents flow in the region of the midlatitude trough characterized by low conductivity, and so are seen as the responsible for the generation of large poleward electric fields, in order to maintain current continuity.

Karlsson *et al.* [1998b] reported results from a statistical study based on Freja satellite measurements. Refinements to the mechanism proposed by Andersen *et al.* [1993] were presented in order to explain the close relationship of the observed SAID events with the midlatitude trough and the currents flowing through this region.

Figure 4.2. is a result presented by Rodger *et al.* [1986], and shows the distribution of the number of midlatitude troughs versus magnetic local time.

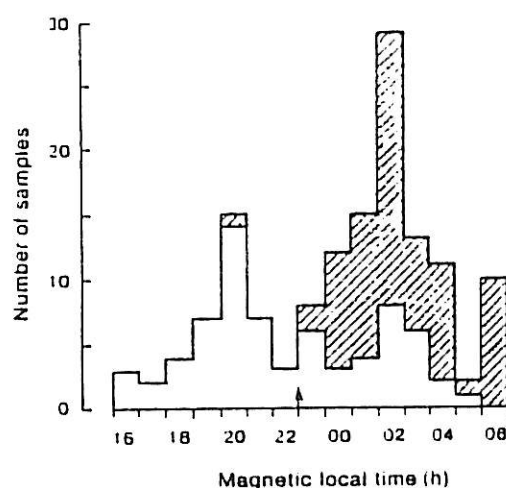


Figure 4.2.
Distribution of number of troughs versus MLT
determined from Dynamics Explorer-2 data.
(From Rodger *et al.*, 1986)

The unshaded region of the plot represents occasions where the difference of location of the poleward edge of the midlatitude trough with respect to the equatorward edge of the energetic (~ 1 keV) particle boundary was less than 0.5.... The shaded region represent occasions where the difference was greater than 0.5....

The predominance of SAID occurrence encountered in the region between 2000 and 2300 MLT shown by Figure 3.3., is in agreement with the distribution of midlatitude trough events found by Rodger *et al.* [1986], represented by the unshaded region. Also in this MLT region, the most intense SAID events were found as shown by Figure 3.4.

This result supports the model of ionospheric current closure through the low conductivity region of the midlatitude trough, as the possible mechanism responsible for the generation of intense poleward electric fields. This is illustrated schematically in Figure 4.3. .

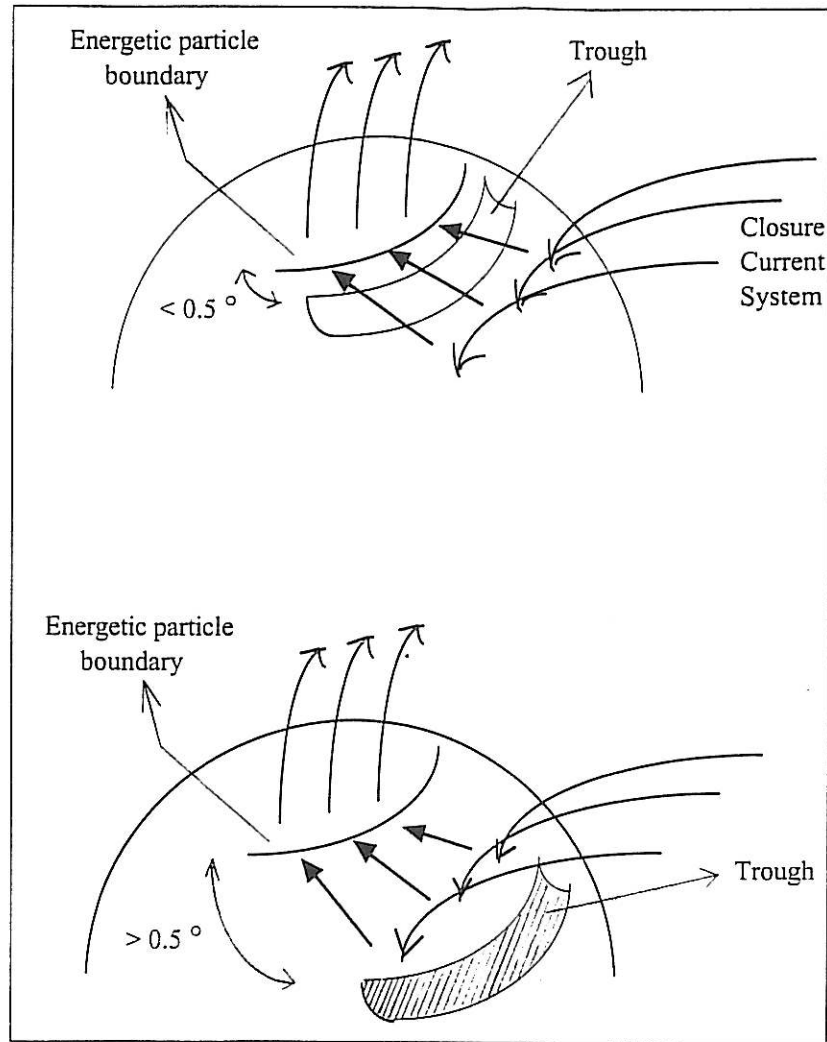


Figure 4.3.
Schematic picture of the closure current system for the two mentioned situations.

From Figure 3.7., it was seen that intense SAID events correspond to small scale-sizes. However the distribution does not show a smooth behaviour, showing instead a rather abrupt change located around 40 km.

This fact makes one wonder about the existence of a threshold electric field value (~ 100 mV/m) characteristic of scale-sizes near 40 km, above which some feedback mechanism is started, leading to the creation of larger electric fields. This feedback mechanism might be related to a decrease on the conductivity due to an increase on the temperature as a effect of Ohmic heating, and so to the recombination rate of some ion species like O^+ . This decrease on the background conductivity induces the requirement of stronger electric fields in order to maintain continuity of ionospheric currents through such structures. Higher electric field magnitudes will then result in an increase on Ohmic heating, giving in this way a continuation to the feedback cycle.

Rodger *et al.* [1992] referred to some consequences for plasma behaviour resulting from the presence of a strong electric field (> 50 mV/m). Three possible processes

were indicated as leading to trough formation. These processes were schematically represented as shown in Figure 4.4.

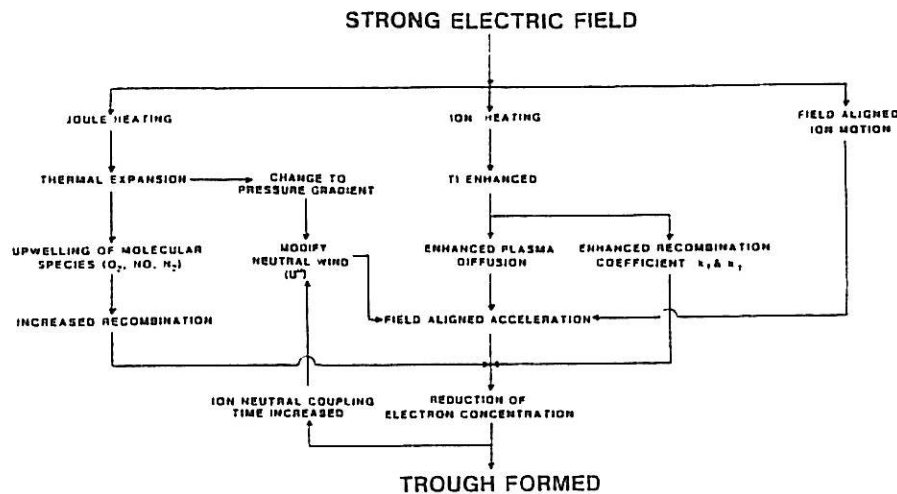


Figure 4.4.

Block diagram illustrating the geophysical processes occurring in a region of strong electric field.

(From Rodger *et al.* [1992])

However these different processes correspond to different time-scales. The most immediate response is ion heating (<1 min), whereas joule heating has a time-scale of the order of 10 minutes to 1 hour.

The lifetime of some SAID events detected by Astrid-2, was found to be more than 1 hour and less than $3\frac{1}{2}$ hours. This coincides with the predicted value by the model of Keyser *et al.* [1998]. However, one event seems to last during approximately 5 hours.

In this way the reaction of the ionospheric plasma to the existence of an intense electric field, seems to induce the creation of several mechanisms that will act on the ambient plasma with different time-scales, changing its composition and consequently leading to the creation of even stronger electric fields.

The reduction of the scale-size that accompanies the generation of larger electric fields, may be considered consistent with the presence of a voltage generator. However, the creation of intense electric fields in the trough region might point towards the existence of a current generator. So, the question pointed out by Anderson *et al.* [1993] remains: Does the magnetosphere behave predominantly like a voltage generator or a current generator?

From the plot shown in Figure 3.7. it was concluded that it takes between 30 to 80 minutes from the start of the substorm expansion phase, to establish the necessary conditions that will induce the generation of a strong poleward electric field.

This time delay might be related to the time duration of a deepening process occurring on the trough, and so reducing the conductivity in this region and consequently creating intense electric fields. The interval 30 to 80 minutes is consistent with the time-scale characteristic of the Joule heating process indicated by *Rodger et al.* [1992] as one of the responsables for trough formation.

This process is illustrated schematically on the picture below.

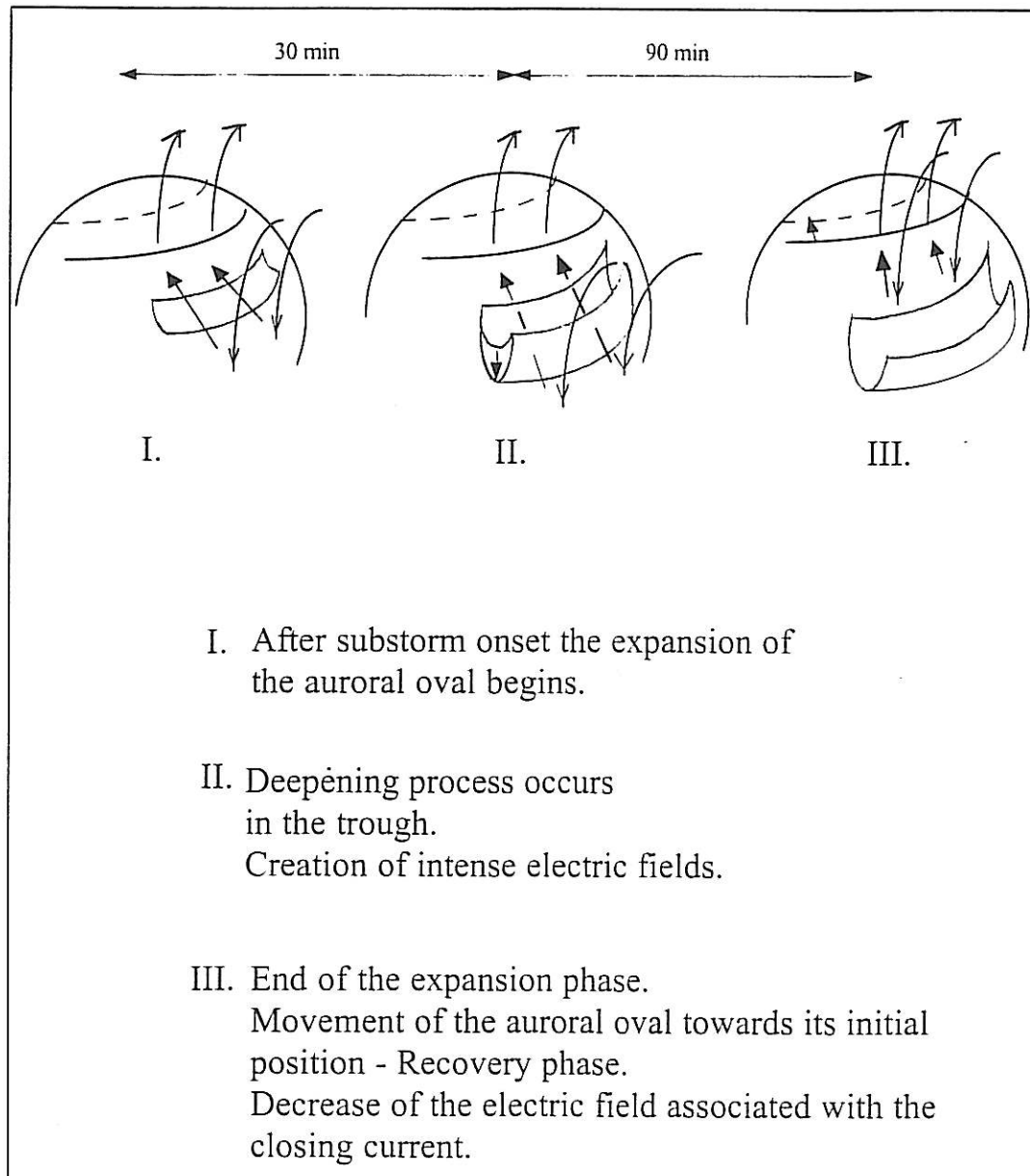


Figure 4.5.
Schematic interpretation of the time delay between the start of the expansion phase and the apparition of a SAID event.

This result is in agreement with the findings reported by *Anderson et al.* [1993], where SAID events were seen to occur more than half an hour after substorm onset. The same value was also predicted by the model of *Keyser* [1999] for the inward travelling time of the injected plasma.

The dependence of occurrence of SAIDs events on the period of the year represented on Figure 3.8., shows that is during the autumn season when are set in the suitable ionospheric and magnetospheric conditions for the generation of more and stronger poleward electric fields. This might be a consequence of the decrease in ambient conductivity characteristic of winter period, and of the increase in magnetic activity during the equinox periods. Strong events were also detected during the spring equinox. The same behaviour was observed by *Karlsson et al.* [1998b].

The dependence of the magnitude of the events on magnetic activity does not show a clear pattern. However, strong events detected during summer season occurred under a high magnetic activity level.

The IMF By dependence was studied based on Figure 3.11. and results show that on the Northern Hemisphere stronger events occur for positive IMF By. On the Southern Hemisphere, the strongest events occurred for negative IMF By.

The results from the statistical study realized by *Karlsson et al.* [1998b] show an opposite behaviour. However, the IMF data used for the present analysis was measured by the WIND satellite which orbit is not always outside the magnetosphere. This fact turns rather questionable the result obtained.

Figure 3.9. shows a tendency for the SAID location to move towards lower latitudes with increasing *Kp*. The same behaviour was reported by *Karlsson et al.* [1999] and predicted by *Keyser* [1999]. Although the trough shows a similar behaviour, the location of the SAID events seems to occur not always collocated with the trough minimum. Several events were detected poleward of the average trough minimum position and few were detected equatorward.

Wondering if this relative position depends on the electric field peak magnitude, results from a rather small statistics done for each magnetic activity interval, show that the strongest SAID events seem to occur poleward of the trough minimum under high magnetic activity conditions, whereas for lower activity levels the strongest events occur collocated with the trough minimum.

This might be related with the existence of a larger separation between the poleward edge of the midlatitude trough and the equatorward edge of the energetic particle boundary, under high magnetic activity conditions. This situation would lead to the creation of the maximum electric field peak poleward to the trough minimum and with a larger scale-size. Under low magnetic activity, this separation would not be so significant and consequently the SAID event appears closer to the trough minimum position and with a narrower peak.

From the case study results presented in section 3.2., the Pedersen conductivity profiles were obtained for five different SAID events. As summarized before, orbits 11882 and 14676 show the maximum electric field peak located poleward to the conductivity minimum. These events occurred under high magnetic activity (*Kp* equal to 6.7 and 5, respectively) and are characterized by a large scale-size (0.40° and 0.42° in CGLat, respectively). The other orbits, 14900, 15827 and 16143, show the

maximum electric field peak collocated with the conductivity minimum. These events occurred under low magnetic activity (Kp equal to 3, 2.7 and 2.7, respectively) and are characterized by smaller scale-sizes (0.28° , 0.25° and 0.28° in CGLat, respectively).

Since the conductivity reduction reflects a depletion on the ionospheric electron density, these results agree with the conclusions and previsions referred about the relative position of the maximum electric field peak and the trough minimum, under different magnetic activity levels.

The field-aligned currents observed have magnitudes between 0.5 and 3 $\mu\text{A}/\text{m}^2$ and correspond to measurements made at altitudes around 1000 km. From field-aligned current density estimates deduced by *Lühr et al.* [1996] values up to 4 $\mu\text{A}/\text{m}^2$ were obtained for altitudes close to 1700 km. *Karlsson et al.* [1998a] indicated values of the order of 10 $\mu\text{A}/\text{m}^2$ ^{simulation values} for the same range of altitudes. *Sugiura et al.* [1982] and *Anderson et al.* [1993] reported values for average current density close to 1.5 $\mu\text{A}/\text{m}^2$ for altitudes around 600 km.

The Pedersen conductivity show values between 0.5 and 10 S. *Sugiura et al.* [1982] presented values for the Pedersen conductivity calculated for altitudes around 600 km, between 3.5 and 7.2 S.

Thus, the values obtained have the same order of magnitude as results from previous studies. The depletion shown by the height-integrated ionospheric Pedersen conductivity near the zone of enhanced electric field, is also consonant with the previsions made by *Anderson et al.* [1993]. This depletion was referred as a consequence of fast chemistry and transport acting on the ionospheric plasma due to frictional heating via collisions with the neutral atmosphere and consequent thermal expansion.

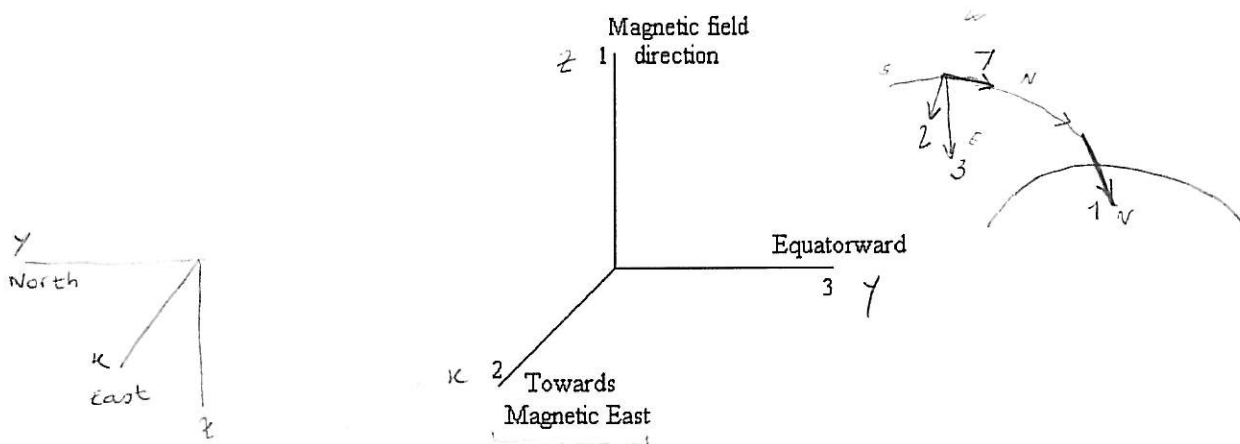
Appendix

Geophysical Coordinate Systems

When studying solar-terrestrial interaction processes it is common to define several different coordinate systems. This is due to the fact that each physical phenomenon is better and easily understood when studied using the appropriate reference system.

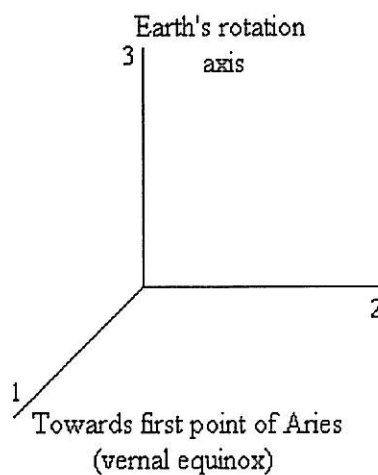
Here it will be summarized the definitions of some coordinate systems commonly used on geophysical studies.

MEE — Magnetic field, East, Equator system



This system is commonly used for describing magnetospheric measurements.

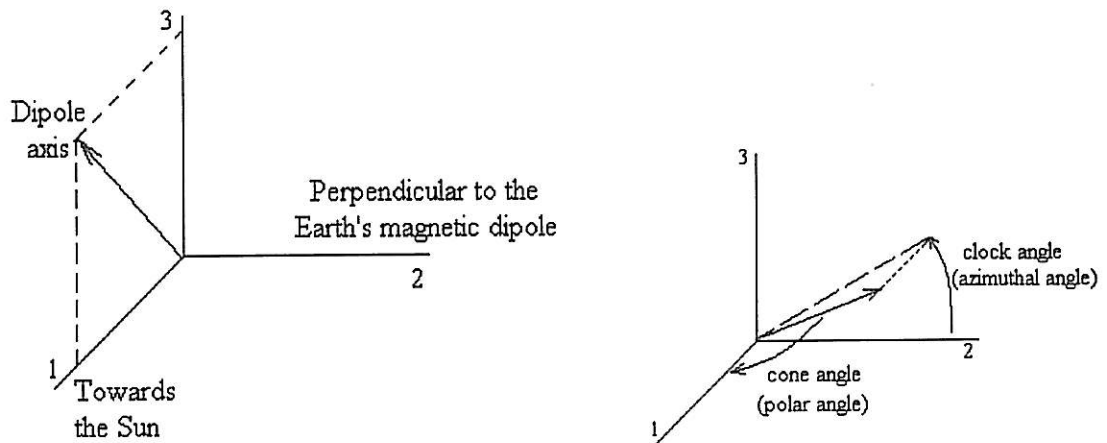
GEI — Geocentric Equatorial Inertial system



The direction of the 1-axis corresponds to the intersection line of the Earth's equatorial plane and the ecliptic plane.

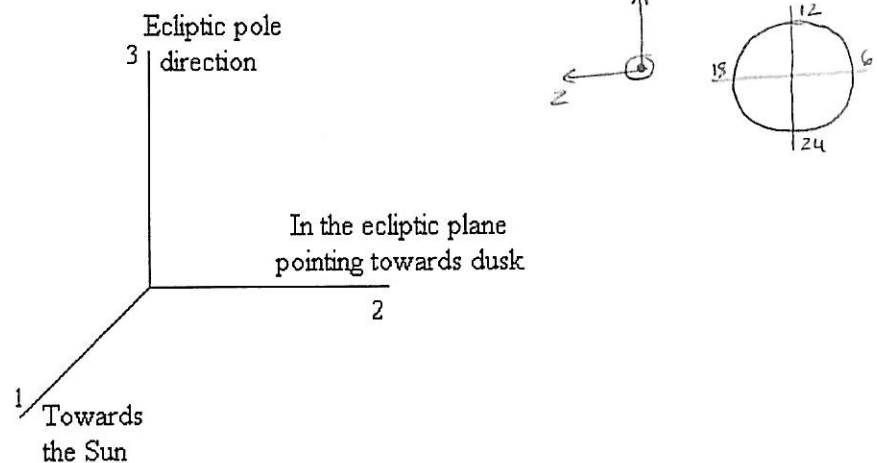
This system is commonly used in astronomy and satellite orbit calculations.

GSM — Geocentric Solar Magnetospheric system



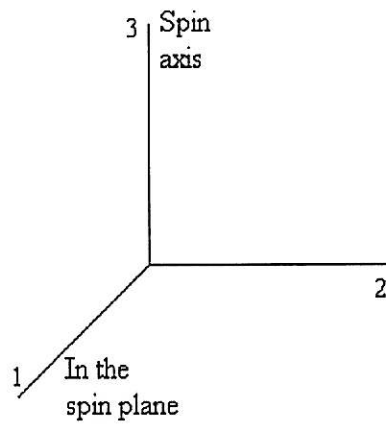
This system is used when describing magnetosheath and magnetotail magnetic fields, magnetosheath solar-wind velocities and models of magnetopause currents.

GSE — Geocentric Solar Ecliptic system

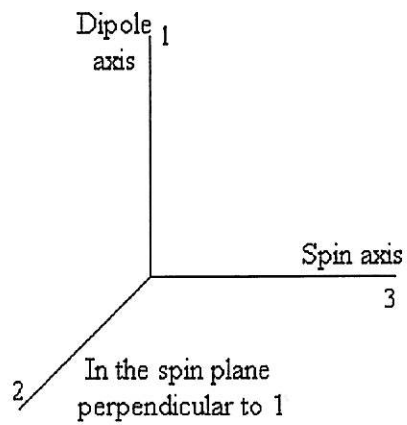


Used to display satellite trajectories, interplanetary magnetic-field observations and data on solar wind.

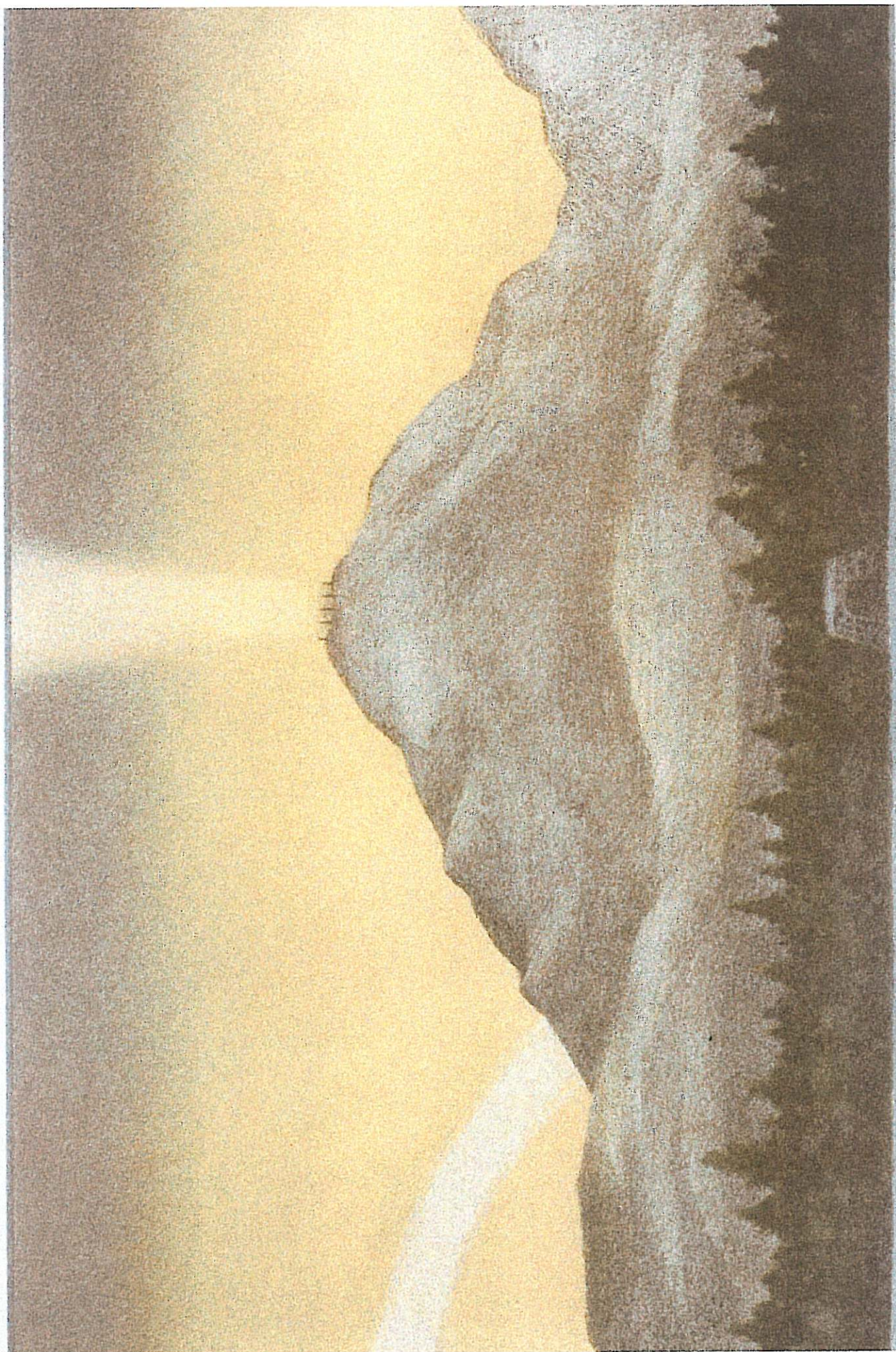
SAT — SATellite system



MSP — Magnetic and Spin Plane system



Both SAT and MSP are used for satellite trajectories description.



Acknowledgements

I would like to thank to Tomas Karlsson for supervising my work and to Professor Göran Marklund for giving me the opportunity to make my degree thesis at the Alfvén Laboratory and also for useful comments on my work.

I am also very grateful to these and other people at the Alfvén Laboratory and to everyone from the Erasmus Programme for making my last ten months in Sweden such a rewarding experience.

Finally, *Um Muito Obrigado* for my family and friends for all their support.

References

- Akasofu, S.-I., Physics of Magnetospheric Substorms, Dordrecht:Reidel, 1977.
- Anderson, P. A., W. B. Hanson, R. A. Heelis, J. D. Craven, N. D. Baker, and L. A. Frank, A proposed production model of rapid subauroral ion drifts and their relation to substorm evolution, *J. Geophys. Res.*, **98**, 6069, 1993.
- Anderson, P. C., R. A. Heelis, and W. B. Hanson, The ionospheric signatures of rapid subauroral ion drifts, *J. Geophys. Res.*, **96**, 5785, 1991.
- André, M. (Ed.), The Freja Scientific Satellite, IRF Scientific Report 214, Kiruna, 1993.
- Best A., Best I., Lehmann H.-R., Johanning D., Seifert W., and Wagner C.-U., in *Proceedings of the Conference Achievements of the IMS, 26-28 June, Graz, Austria*, ESA SP-217, 1984.
- Burton, R. K., McPherron, R. C., and Russell, C. T., The Terrestrial Magnetosphere: A Half Wave Rectifier of the Interplanetary Electric Field, *Science*, **189**, pp. 717-718, 1975.
- Hanson, W. B., Structure of the Ionosphere, in *Satellite Environment Handbook*, F.S. Johnson (Ed.), Stanford University Press, 1965
- Johnson, C.Y., Ion and neutral composition of the ionosphere. *Annals of the IQSY*, **5**:197-213, 1969.
- Karlsson, T., and G. Marklund, Simulations of Effects of Small-scale auroral Current Closure in the Return Current Region, *Physics of Space Plasmas*, **15**, 401, 1998a.
- Karlsson, T., G. T. Marklund, L. G. Blomberg, and A. Mälkki, Subaural electric fields observed by the Freja satellite: A statistical study, *J. Geophys. Res.*, **103**, 4327-4341, 1998b.
- Keyser, J. De, Formation and evolution of subauroral ion drifts in the course of a substorm, *J. Geophys. Res.*, **104**(A6):12,339-349, 1999.
- Keyser, J. De, M. Roth, and J. Lemaire, The magnetospheric driver of subauroral ion drifts, *Geophys. Res. Lett.*, 1998.
- Kivelson, M. G., and C. T. Russell, Introduction to Space Physics, Cambridge University Press, 1995.
- Lühr H., J. F. Warnecke, and M. K. A. Rother, An Algorithm for Estimating Field-Aligned Currents from Single Spacecraft Magnetic field Measurements: A Diagnostic Tool Applied to Freja Satellite Data, *IEEE Transactions on Geoscience and Remote Sensing*, **34**, 1369-76, 1996.
- Lemström, Selim, Om polarljuset eller norrskenet, 1886

McPherron, R. L., Magnetospheric substorms, *Rev. Geophys. Space Phys.*, 17(4):657-81, 1979

McPherron, R. L., Physical processes producing magnetospheric substorms and magnetic storms, in *Geomagnetism*, vol4, ed. J. Jacobs (pp. 593-739), London Academic Press, 1991.

McPherron, R. L., and R. H. Manka, Dynamics of the 1054 UT, March 22, 1979 substorm event: CDAW-6, *J. Geophys. Res.*, 90(A2):1175-90, 1985.

Rodger, A. S., R. J. Moffett, and S. Quegan, The role of ion drift in the formation of ionization troughs in the mid- and high-latitude ionosphere—a review, *J. of Atmosph. and Terr. Phys.*, 54, 1-30, 1992.

Rostoker, G., S.-I. Akasofu, J. Foster, R. A. Greenwald, Y. Kamide, K. Kawasaki, A. T. Y. Lui, R. L. McPherron, and C. T. Russell, Magnetospheric substorms — definition and signatures, *J. Geophys. Res.*, 85(A4):1663-8, 1980.

Sandahl, Ingrid, Norrskén: Budb rare från rymden, Atlantis, 1998.

Spiro, R. W., R. H. Heelis, and W. B. Hanson, Rapid sub-auroral ion drifts observed by Atmospheric Explorer C., *Geophys. Res. Lett.*, 6, 657, 1979.

Sugiura M., N. C. Maynard, W. H. Farthing, J. P. Heppner, and B. G. Ledley, Initial results on the correlation between the magnetic and electric fields observed from the DE-2 satellite in the field-aligned current regions, *Geophys. Res. Lett.*, 9(9):985-988, 1982.

